

Alma Mater Studiorum Università di Bologna  
Archivio istituzionale della ricerca

Observational analysis of an exceptionally intense hailstorm over the Mediterranean area: Role of the GPM Core Observatory

This is the final peer-reviewed author's accepted manuscript (postprint) of the following publication:

*Published Version:*

Marra, A.C., Porcù, F., Baldini, L., Petracca, M., Casella, D., Dietrich, S., et al. (2017). Observational analysis of an exceptionally intense hailstorm over the Mediterranean area: Role of the GPM Core Observatory. *ATMOSPHERIC RESEARCH*, 192, 72-90 [10.1016/j.atmosres.2017.03.019].

*Availability:*

This version is available at: <https://hdl.handle.net/11585/584431> since: 2021-03-08

*Published:*

DOI: <http://doi.org/10.1016/j.atmosres.2017.03.019>

*Terms of use:*

Some rights reserved. The terms and conditions for the reuse of this version of the manuscript are specified in the publishing policy. For all terms of use and more information see the publisher's website.

This item was downloaded from IRIS Università di Bologna (<https://cris.unibo.it/>).  
When citing, please refer to the published version.

(Article begins on next page)

This is the final peer-reviewed accepted manuscript of:

C. Marra, F. Porcù, L. Baldini, M. Petracca, D. Casella, S. Dietrich, A. Mugnai, P. Sanò, G. Vulpiani, G. Panegrossi, *Observational analysis of an exceptionally intense hailstorm over the Mediterranean area: Role of the GPM Core Observatory*, Atmospheric Research, Volume 192, 1 August 2017, Pages 72-90.

The final published version is available at:  
<https://doi.org/10.1016/j.atmosres.2017.03.019>

#### Rights / License:

The terms and conditions for the reuse of this version of the manuscript are specified in the publishing policy. For all terms of use and more information see the publisher's website.

This item was downloaded from IRIS Università di Bologna (<https://cris.unibo.it/>)

**When citing, please refer to the published version.**

# **Observational analysis of an exceptionally intense hailstorm over the Mediterranean area: Role of the GPM Core Observatory**

A.C. Marra<sup>a</sup>, F. Porcù<sup>b</sup>, L. Baldini<sup>a</sup>, M. Petracca<sup>c,d</sup>, D. Casella<sup>e</sup>, S. Dietrich<sup>a</sup>,  
A. Mugnai<sup>a</sup>, P. Sanò<sup>a</sup>, G. Vulpiani<sup>c</sup>, and G. Panegrossi<sup>a</sup>

<sup>a</sup> Institute of Atmospheric Sciences and Climate (ISAC), Italian National Research Council (CNR)  
00133 Rome, Italy

<sup>b</sup> Department of Physics and Astronomy, University of Bologna  
40127 Bologna, Italy

<sup>c</sup> Department of Civil Protection (DPC), Presidency of the Council of Ministers  
00189 Rome, Italy

<sup>d</sup> Department of Physics and Earth Science, University of Ferrara  
40122 Ferrara, Italy

<sup>e</sup> SERCO S.p.A.  
00044 Frascati, Italy

Submitted to **Atmospheric Research**

Revised version February 2016

## **\* Corresponding Author:**

Dr. Giulia Panegrossi  
*e-mail:* g.panegrossi@isac.cnr.it  
ISAC-CNR  
Area della Ricerca di Tor Vergata  
Via del Fosso del Cavaliere, 100  
00133 Rome, Italy

## ABSTRACT

On 5 September 2015 a violent hailstorm hit the Gulf and the city of Naples in Italy. The storm originated over the Tyrrhenian Sea dropping 7-10 cm diameter hailstones along its path. During its mature phase, at 08:47 UTC, the hailstorm was captured by one overpass of the Global Precipitation Measurement mission Core Observatory (GPM-CO) embarking the GPM Microwave Imager (GMI) and the Ka/Ku-band Dual-frequency Precipitation Radar (DPR). In this paper, observations by both GMI and DPR are thoroughly analysed in conjunction with other spaceborne and ground-based measurements, to show how the GPM-CO integrates established observational tools in monitoring, understanding, and characterizing severe weather. Rapid-scan MSG SEVIRI images show an extremely rapid development, with 10.8  $\mu\text{m}$  cloud-top temperatures dropping by 65 K in 40 minutes down to 198 K. The Lightning NETWORK registered over 37000 strokes in 5 hours, with intracloud positive strokes fraction increasing during the regeneration phases, when ground-based polarimetric radar and DPR support the presence of large graupel/hail particles. DPR Ku 40 dBZ and 20 dBZ echo top heights at 14 km and 16 km, respectively, indicate strong updraft and deep overshooting. GMI extremely low brightness temperatures (TBs) in correspondence of the convective core (158, 97, 67, and 87 K at 19, 37, 89 and 166 GHz) are compatible with the presence of massive ice particles. In two years of GPM global observations the storm ranks as fourth and first in terms of minimum 37 and 19 GHz (V-pol) TBs, respectively. This study illustrates GPM-CO sensing capabilities for characterizing the structure of such severe hailstorm, while providing observational evidence of its intensity and rarity, globally, and, in particular, in the Mediterranean area.

**Keywords:** GPM, Mediterranean, hailstorm, extreme events, remote sensing, lightning

## 1. Introduction

The Mediterranean is a unique meteorological environment and a weather forecasting challenge, and is recognized as one of the major climate hot-spots in the world (Giorgi, 2006). In this region severe weather events of different nature, such as deep convective systems (Manzato et al., 2014), sometimes mesoscale organized (Romero et al., 2015; Panegrossi et al., 2016), cut-off lows (Kotroni et al., 2006; Porcù et al., 2007), intense extratropical (Tripoli et al., 2005; Flaounas et al., 2015) and tropical-like cyclones (Reale and Atlas, 2001; Emanuel, 2005; Miglietta et al., 2013; Cavicchia et al., 2014) often originate over the relatively warm sea and develop to hit coastal areas, often rich in assets and densely populated, causing major damages and casualties (Porcù et al., 2003, Llasat et al., 2013).

A number of studies has recently been devoted to severe weather events over the Mediterranean area, both from the observational (Di Paola et al., 2014; Bech et al., 2015; Vulpiani et al., 2015; Roberto et al., 2016; Panegrossi et al., 2016) and numerical modelling (Cohuet et al., 2011; Buzzi et al., 2014; Cassola et al., 2015) points of view, addressing also their impact on the ground (Silvestro et al., 2015). In addition, over the last decade several coordinated international efforts have focused on the observation and forecasting of severe weather over the Mediterranean area: European projects such as EURAINSAT (Levizzani et al., 2007), MEDEX (Jansa et al., 2014), RiskMed (Bartzokas et al., 2010), FLASH (Price et al., 2011), or experiments such as HyMeX (Drobinski et al., 2014, Ferretti et al., 2014), together with the dedicated series of Plinius Conference on Mediterranean Storms/Risks of the European Geosciences Union (<http://www.egu.eu/meetings/conference-series/plinius-topical-conferences/>) have substantially improved knowledge and forecasting skills over such area.

The complex orography of the Mediterranean coastal regions, and the need to monitor severe events during their offshore development, make the use of conventional ground-based instruments (e.g., raingauges and weather radar networks) inadequate to provide the observational details that are necessary to improve the monitoring and forecasting of severe weather in terms of time, location, and strength (Panegrossi et al. 2016). On the other hand, lightning data can help monitoring and analyzing the evolution of convective storms, particularly of their most intense phases. Many studies over the past decades have been carried out to correlate lightning occurrence and/or polarity to severe weather often with inconclusive and contrasting results (e.g. Schultz et al., 2011 and references therein). Moreover, the use of satellite measurements can be used as a further tool to study severe events over the sea and large part of the coastal regions. Most of the studies reported in literature focus on the capability of remote sensors to estimate precipitation, as one of the major environmental issues linked to the development of severe weather, but only few efforts have been

devoted to increase the knowledge of structure and dynamics of such cloud systems.

The VISible-Near-InfraRed-InfraRed (VIS-NIR-IR) sensors available in the last decade at geostationary scales with relatively high temporal sampling (15 minutes and less) and ground resolution (3 to 5 km at nadir) and with constantly improving radiometric capabilities, provide unprecedented data to study cloud upper level structure and dynamics. By using the reflectance in the VIS-NIR part of the spectrum it is possible to estimate cloud optical thickness and cloud top particle effective radius (Nakajima and Nakajima, 1995), and to link these properties to the cloud vertical structure (Rosenfeld and Lenski, 1998). This information allowed a detailed study of cloud top features, such as plumes (Levizzani and Setvak, 1996; Melani et al., 2003), spots and U/V shapes (Setvak et al., 2007). A systematic use of geostationary IR brightness temperature (Mecikalski et al, 2010a) and VIS-NIR reflectance (Mecikalski et al., 2010b) linear combinations and temporal properties allows to estimate growing convective clouds properties.

While VIS/IR frequencies are not best suited to obtain information on precipitation and cloud vertical structure, Passive MicroWave (PMW) radiometers on board low-Earth-orbit (LEO) satellites have been largely used to extract quantitative information on precipitation and bulk cloud structure, since the upwelling radiation responds to cloud and precipitation microphysics, besides the surface, as shown in the early studies by Mugnai et al. (1990), Smith et al. (1994); Kummerow et al. (1996), Panegrossi et al. (1998) based on combined cloud resolving model and radiative transfer simulations. However, the impossibility to continuously monitor cloud evolution by means of LEO satellites, as well as the generally large footprints of PMW measurements and the strong surface signal, represent actual limitations in the use of such sensors for a full understanding of cloud structure properties. The launch of the first precipitation radar on board the Tropical Rain Measuring Mission (TRMM, Kummerow et al., 2000) opened new possibilities to study tropical cloud structures, with special emphasis on precipitation (Jiang et al., 2011), and its climatological spatial distribution (e.g. Nesbitt et al., 2000; Cecil et al., 2005), with a particular focus on deep convection (e.g. Liu and Zipser, 2005; Zipser et al., 2006). The Cloud Profiling Radar (CPR) on the CloudSat mission, launched in 2006 (Stephens et al, 2008), was designed to assess at quasi-global scale cloud abundance, distribution, structure, and radiative properties, to understand the role of clouds in climate. Given its sensitivity to small cloud particles (and the strong attenuation by high water content) was used to study non-precipitating clouds (Lee et al., 2010) and to estimate snowfall rate (Kulie and Bennarz, 2009).

With the advent of the NASA/JAXA Global Precipitation Measurement (GPM) mission (Hou et al., 2014) a new era has started for cloud studies and precipitation monitoring from space. The constellation of satellites carrying PMW radiometers has now reached an optimal configuration,

ensuring a 3-hourly global coverage, and is now completed by the GPM Core Observatory (GPM-CO), successfully launched in February 2014. The GPM-CO is the primary rain-measuring satellite equipped with two instruments: the Dual Precipitation Radar (DPR), a dual-frequency Ku/Ka-band radar, and the GPM Microwave Imager (GMI), a high resolution, conically scanning multichannel PMW radiometer. GMI and DPR are the reference satellite-borne instruments for the retrieval of precipitation and cloud microphysical structure, providing consistent observations around the globe at all latitudes between 68°S and 68°N. Besides the GPM-CO, the other constellation satellites are equipped with cross-track or conically scanning PMW radiometers with appropriate sets of precipitation sensing channels. An example of the use of the GPM constellation for monitoring heavy precipitation events over the Mediterranean region can be found in Panegrossi et al. (2016). The first-year observations of GPM-CO have been used to create a true global map of the largest, deepest and most intense precipitation systems (Liu and Zipser, 2015).

In this study the GPM-CO observations of a violent hailstorm, that developed over the Tyrrhenian Sea and hit the Gulf and the city of Naples in Italy on 5 September 2015 (hereinafter referred to as the Naples hailstorm) are thoroughly analysed and discussed, in conjunction with other satellite and ground-based measurements. We illustrate the unprecedented capabilities of the GPM-CO satellite for characterizing the structure of this exceptionally severe storm. We show that the combined use of measurements from GMI and DPR with those available from other sensors provides observational evidence of extremely rare features of the Naples hailstorm, while demonstrating the potential of GPM-CO to enhance the understanding of these severe convective systems by providing unique spaceborne measurements of the 3-D structure of precipitation. The purpose of this work is to show that the use of advanced cross cutting observational tools, combining data from different platforms, is essential for the characterization of such severe and rapidly evolving convective systems, which periodically devastate the Mediterranean coastal regions, and to document how the GPM integrates the established observational ground-based and satellite-borne tools in monitoring, understanding, and characterizing severe weather.

## **2. Observational dataset description**

The Naples hailstorm originated from a southward plunge of the jet stream that carved into Western Europe, sending an upper disturbance into the Italian peninsula. That instability, associated with high Sea Surface Temperature (SST), and low-level convergence, stirred up an impressive severe thunderstorm with intense lightning activity and strong winds, that started developing before 06:00 UTC over the Tyrrhenian Sea off the coast of Naples, and reached maturity by 06:37 UTC, hitting the coast around 09:00 UTC, moving inland afterwards, until its complete dissipation around 12:00

UTC. The storm was exceptionally violent, dropping 7-10 cm diameter hailstones along its path over the sea (see Fig. 1) and over land.

## **2.1 MSG, lightning, and ground-radar**

In this study Meteosat Second Generation (MSG) Spinning Enhanced Visible and Infrared Imager (SEVIRI) data (Schmetz et al., 2002) are used with two main purposes: to study the cloud top structures and to analyse the growth of the first stages of cloud life, taking advantage of the Rapid Scanning Service (RSS) 5-minute acquisition. SEVIRI observes the Earth in 12 spectral channels: we analysed the High Resolution Visible (HRV), and the 10.8  $\mu\text{m}$  (IR) channels, with 1x1 and 3x3 km resolution at nadir, respectively.

In addition, lightning data from the ground-based low-frequency (VLF/LF) Lightning Network (LINET) network are used to analyze the evolution of the hailstorm. LINET system covers a wide area from approximately 30°N 10°W to 65°N 35°E and detects the total lightning, but it is also able to discriminate between cloud-to-ground strokes (CG) and intra-cloud lightning (IC), and their polarity (positive IC+ and CG+, and negative IC- and CG-) (Betz et al., 2004; Betz et al., 2009). The 3D discrimination method is reliable (with a position accuracy of 150 m) when the sensor baseline does not exceed ~200 km. Moreover LINET allows for estimation of IC emission height, although at least 4 sensors are needed for a reliable determination of the IC strokes height (Betz et al., 2004, Höller et al., 2009). In this study the information provided by LINET is fully exploited; specifically, the time (with temporal resolution of about 512 ms), horizontal and vertical location of VLF-sources, as well as the polarity of IC and CG strokes.

The Naples hailstorm was observed by the operational dual polarization weather radar (hereinafter GR) located in Monte il Monte (41.94°N, 14.62°E, 710m ASL) managed by the Civil Protection Department of Italy. The GR was scanning according to a strategy including a sequence of 12 sweeps at the elevation angles of 90°, 16°, 13.5°, 11°, 9°, 7°, 5.5°, 4.6°, 3.5°, 2.5°, 1.5°, 0.5°. The development of the hailstorm occurred at a distance between 100 and 150 km away from the GR. Due to the interception of GR beam by the peaks of the Apennine range, measurements from sweeps at the lowest elevation angle (0.5°) are affected by some percentage of beam screening. Starting from elevation angles of 1.5°, the GR sector interested by the hailstorm was not affected by beam blocking. The nominal range resolution is 150 m for all the elevation angles, with the exception of the scan along the vertical, whose resolution is 100 m. Measurements of radar reflectivity factor at horizontal polarization ( $Z_h$ ), differential reflectivity ( $Z_{dr}$ ), and copolar correlation coefficient ( $\rho_{hv}$ ) are available for this case. Incidental and unexpected unavailability of differential phase shift does not allow us to compensate for C-band attenuation in a reliable manner



and to use this measurement for particle investigation. Attenuated measurements of  $Z_h$  and  $Z_{dr}$  are used in this work but mainly focusing on their spatial variability.

## **2.2 GPM constellation: GPM-CO and MHS**

The GPM-CO captured the hailstorm at its mature stage, at 08:47 UTC at 40.79°N, 13.86°E on a descending orbit. The most intense portion of the storm was approaching the coast, in the center of the 904 km wide GMI swath and of the narrower cross-track DPR swath (245 and 120 km wide for the Ku- and Ka-band radar, respectively). GMI offers the richest set of microwave frequencies available, with 10 dual-polarization window channels at 10, 19, 36.5, 89, and 166 GHz, and three single polarization water vapor absorption channels (one at 23.8 GHz and two at 183.31 GHz). Moreover, GMI provides PMW measurements at a constant viewing angle (off-nadir-angle of 48.5° corresponding to an earth-incidence-angle of 52.8°) at the highest available spatial resolution among the GPM constellation of radiometers (i.e. up to roughly 4 km x 7 km at the high frequency channels and around 11 km x 18 km at 19 GHz).

Besides the GPM-CO overpass, two overpasses from the cross-track scanning Advanced Microwave Sounding Unit–A/Microwave Humidity Sounder (AMSU-A/MHS) were available: the first one by MetOp-A at 08:34 UTC at 40.99°N, 13.64°E, 13 minutes before the GPM-CO overpass, and the second one by MetOp-B at 09:28 UTC at 40.84°N, 14.35°E, when the storm had moved over land. In this study we use only measurements from MHS, which is equipped with five channels: three channels in the 183.31 GHz water vapor absorption band, and two window channels at 89 and 150 GHz. The MHS measurements are available on a 2343 km wide swath with spatial resolution which varies along the scan degrading from nadir to the edge (from around 16 km x 16 km to 26 km x 52 km for all channels) while polarization (V/H) information is not available from the mixed polarization signal. In this study, the NASA/JAXA GPM official data are used. In particular we have used version 4 (V04) of Level 1C-R product [common calibrated brightness temperatures (TBs) with the low-channel pixels matched to the nearest neighbor high-channel pixel] for GMI, Level 1C product (common calibrated TBs) for MHS, and 2A-DPR product for Ku-band and Ka-band reflectivity. Only the measured (not corrected) reflectivity factor (hereinafter  $Z_m$ ) is used in this study, because a number of issues were found in the corrected reflectivity provided with the DPR products. It is worth pointing out that for such intense (and rare) hailstorms it is very difficult to correct for attenuation, because the distribution of hail is unknown and not uniform, and because of the effects of multiple scattering in presence of graupel or hailstones (Battaglia et al., 2015). These effects are not fully accounted for in DPR products version 4 (Iguchi, private communications).

### 3. Analysis and discussion

#### 3.1 Temporal evolution of the storm as inferred by MSG IR, lightning and ground radar observations

MSG SEVIRI data are useful to describe the early stages of the storm development, since no other available observations could resolve the cloud initiation. Cloud top features are investigated through the HRV reflectance to detect the appearance and location of the overshooting top and plumes. The IR channel radiance, converted in equivalent black body temperature, is used to observe the thermal structure of cloud top and to monitor the growth phase of the system, focusing on the convective initiation and early stages, by observing how and how fast cloud top brightness temperatures vary with time at the RSS sampling rate (5-min), also in relation to the lightning activity.

Figure 2 shows the life cycle of the storm (from the early stages to its mature phase) through a sequence of eight SEVIRI snapshots reported using the “sandwich” visualization technique (Manzato et al, 2014), to enhance the cloud top topography and thermal structure, by merging the HRV and IR information. In this figure key features of the storm evolution phases are highlighted along with the time of the other observations available (LINET, LEO satellite, and GR).

SEVIRI images show an isolated thunderstorm which quickly developed over the eastern Mediterranean Sea [Fig. 2, panels a) and b)] and moved eastward across central Italy [Fig. 2, panels c) through h)]. . At 07:52 UTC (Fig. 2 left panel d)) a well-structured “split plume” is detected (yellowish colours), originating downwind the overshooting top (dark red spot), that is usually referred as supercell signature (Levizzani and Setvák, 1996). The sandwich images at 08:37 UTC (close to MetOp-A overpass), 08:47 UTC (time of the GPM-CO overpass), and at 09:32 UTC (close to MetOp-B overpass) [Fig. 2 panels e), f), and g)] show a growing anvil moving to NE. At the time of the GPM overpass the most active part of the storm is on the coast.

In Fig. 3 the time series of cloud top features are reported to monitor the cloud growth and to estimate the updraft speed in the early stages, i.e. before the cloud top reaches the tropopause, which is around 210 K, as inferred by the Pratica di Mare (41.65°N, 12.43°E) radiosounding at 00:00 UTC (not shown). We considered the SEVIRI IR image where the first cluster of lightning was observed and selected the minimum temperature in this area as the signal of the more intense updraft current (defined as Updraft Top Temperature, UTT) and tracked forward the minimum to record its value and position. As for the time before the lightning initiation, we applied a backward auto-correlation algorithm to monitor the history of the UTT in the early stage of the cloud

development. The IR images are preprocessed with a 3x3 mean filter to make the tracking algorithm more stable: the UTT time series is reported in Fig. 3a, and its time rate of change in Fig. 3b.

The cloud-top IR brightness temperature reached its first minimum at 06:37 UTC, while the absolute UTT minimum was 197.9 K at 07:12 UTC. Once the updraft current reaches the tropopause, hydrometeors spread horizontally, increasing the size of the cloud top area as seen by IR. To follow the growth of the cloud, we considered the size of the cloud area colder than 215 K, 5 K warmer than tropopause, to include some locally warmer part of the inner anvil area. We computed the cloud top divergence (CTD) (Sikdar et al., 1970) as the relative rate of change of the cloud top area at the level of outflow, as defined by the 215 K isotherm on the IR images. Results are shown in Fig. 3c from 06:17 UTC (first appearance of at least one pixel colder than 215 K). Finally, the stroke density (computed as the number of strokes recorded in 5 min intervals on a 1 km<sup>2</sup> area), is reported in Fig. 3d (as strokes per minute per km<sup>2</sup>).

The first clear signal of the main convective updraft shows up in the 05:57 UTC image. The cooling rate of the updraft top is around 1 K min<sup>-1</sup> at the beginning (see Fig. 3b), and reaches its maximum of 4.5 K min<sup>-1</sup> around 06:02 UTC, that, compared to the radiosounding of Pratica di Mare, yield an estimate of the updraft speed around 11.8 m s<sup>-1</sup>. This value has to be assumed as an underestimate of the maximum updraft speed, given the inherent uncertainties in the satellite observation: following the approach of Adler and Fenn (1979) to correct these uncertainties, a consistent estimate of the “true” peak updraft speed is around 50 m s<sup>-1</sup>, compatible with the presence of 8-10 cm sized hailstones at the ground.

The first detection of a cloud top pixel colder than 215K is at 06:17 UTC, indicating the updraft reached the equilibrium level. In the following minutes the cloud top area at the tropopause grows, with an increasing rate. Following the simple model introduced by Sikdar et al (1970), the CTD is proportional to the vertical mass transport due to the convective development: the CTD is higher in the early stages of the cloud life, and then decreases to become very close to zero at 07:17 UTC.

The cloud starts to produce lightning at 06:07 UTC, five minutes later than the maximum UTT cooling rate and ten minutes before the cloud top reaches the tropopause. Then the strokes rate density rapidly increases to reach its maximum within 75 minutes, at 07:22 UTC, to drop down of a factor near 2 in the following 5 minutes, while the UTT remains almost constant, around 205-210 K. The CTD reduces to the 15% of the early stage value, indicating a lower mass flux to the cloud top (Sikdar et al., 1970) that, combined to the high precipitation rate (expected at this stage of the cloud life), could result in a decrease of the ice mass of the cloud. Lightning activity has new relative maxima in the following minutes, probably due to the development of new cells under the

main anvil that are not detected by cloud top temperature analysis.

Because of the very close relationships between the stage of the convective activity and the lightning type and polarity (Williams et al., 1989) and thanks to the availability of this information from LINET, the temporal evolution of the different types of registered strokes during the event is analyzed. A clear indication of the storm severity is provided by the very high number of total (IC and CG) strokes (37220) registered from the lightning initiation at 06:12 UTC until 11:00 UTC. Figure 4 shows that the convective core of the storm moves from West to East, with a very intense lightning activity confirmed by the high number of LINET strokes registered every hour (and rate), reported in Table 1. The most intense electrical activity occurs between 07:00 UTC and 09:00 UTC, when the mean (IC+CG) rate reaches values of about 3 strokes per second (see also Fig. 3d). Figure 4 also shows that often the lightning tracks bifurcate, indicating the possible storm splitting in right- and left- mover storm (Houze et al., 1993), with the latter one more intense, with higher flash occurrence than the first one.

A large IC stroke rate (peaks up to  $150 \text{ min}^{-1}$ ) and an unusually high IC/CG ratio (0.86 from 06:12 UTC throughout 11:00 UTC) are found for this storm compared with other events registered by LINET in the same area (Roberto et al., 2016) and reported in other studies (e.g., Holler et al., 2009). It is worth noting that the number of IC strokes is usually underestimated, due to their lower discharge current compared to CG strokes (e.g., Formenton et al., 2013). The temporal evolution of the lightning activity shown in Fig. 5 (top panel) indicates that in the first minutes CG- strokes are predominant, then CG+ strokes appear, and at the mature stage of the storm IC stroke rate (and IC/CG ratio) increases rapidly.

The highest IC+ fraction peaks (around 0.60 and 0.55 respectively) (Fig. 5, middle panel) are found around 08:45 UTC (close to the time of the GPM overpass) and 10:00 UTC (when hail is reported in the Pozzuoli area). Between 08:45 UTC and 10:00 UTC the IC- fraction also increases, while the CG fraction shows two depressions in correspondence of the IC+ peaks. Another lower peak of IC+ is found around 10:30 UTC, when also the CG- fraction rapidly increases. The only relevant IC- peak is observed between 10:12 UTC and 10:20 UTC. The cyclic variations in the IC and CG fraction within a storm, with periods of high IC activity and low CG activity and *viceversa*, have been observed and associated with the lifetime duration of thunderstorm cells (e.g. Brook and Kitagawa, 1960). Between 08:00 UTC and 11:00 UTC the mean of the IC (IC+) fraction reaches the value of 0.55 (0.41), thus indicating the dominant role of the IC events during the most intense phases of the storm. Moreover, between 07:30 UTC and 10:00 UTC the ratio of CG+/CG- is about 1, while it is always lower than 1 before and after. This time interval is almost coincident with the most intense phase of the hailstorm.

1 A comparison of the electrical activity with reports of hail and rain at the surface seems to indicate a  
2 strong temporal correlation between the IC+ peaks around 09:00 UTC, when large hailstones falling  
3 over the sea off the coast of Naples were observed (Fig. 1), and around 10:00 UTC with the hail  
4 report in the area of Pozzuoli (40.83°N, 14.11°E). The lower IC+ peak around 10:30 UTC,  
5 corresponding also to the increase of CG- against a decrease of CG+, is quite close in time and  
6 space with the report of heavy rain, mixed with smaller hail, at the surface.

7 The IC+ stroke density and emission mean height per minute, are shown in Fig. 5 (bottom panel).  
8 The first peak of IC+ stroke density (and rate, see upper panel) occurs at the time when the IR  
9 reaches the minimum temperature (197.9K at 07:22 UTC), and the maximum IC+ density and  
10 height are found around 09:00 UTC (close to the time of the GPM overpass). It is worthwhile to  
11 note that LINET system has been targeted at discriminating IC and CG strokes rather than precise  
12 height mapping of IC emission events (Betz et al., 2004), and IC emission height may be affected  
13 by significant overestimation (Holler et al. 2009). Nonetheless, an interesting correlation is  
14 observed between the rate (and density) and the mean height of the IC+ strokes. This is particularly  
15 evident around 10:00 UTC and 10:30 UTC, but to some extent, also between 08:30 UTC and 09:30  
16 UTC. Moreover, an analysis of the most frequent IC+ and IC- emission heights (not shown)  
17 indicates that the modal values of IC+ height is always higher than that of IC- (e.g. 11.65 km vs.  
18 7.11 km, respectively, between 08:32 UTC and 09:24 UTC). In spite of the limitations in the  
19 accuracy of IC height mapping by LINET, it can be concluded that IC+ height variability and its  
20 correlation with the IC+ density seem to reflect well the Naples hailstorm evolution phases as  
21 inferred from the GR and local hail reports. This is an interesting result, linked to the strength of the  
22 updraft and to the microphysical structure of the Naples hailstorm, and it will be further analyzed in  
23 Section 3.2.3.

24 Figure 6 shows the evolution of the hail cell as seen by sweeps collected by the Monte il Monte  
25 radar at the 1.5° elevation angle, the lowest one unaffected by beam blocking in the sector of the  
26 hailstorm. Such sweeps are collected with 4-minute delay with respect to the nominal time.  
27 Reflectivity maps are cleaned from ground clutter and the numerous C-band interferences, but not  
28 corrected for propagation attenuation. Measurements at 08:35 UTC (time of MetOp-A overpass)  
29 and 08:45 UTC (time of the GPM-CO overpass) highlight an intense core with  $Z_h > 60$  dBZ.  
30 Subsequent stages point out the split of the cell in two, visible in the panel of 09:30 UTC (time of  
31 MetOp-B overpass) and 1000 UTC (hail reported in the Pozzuoli area, 40.83°N, 14.11°E). Southern  
32 cell survives at later stages, still presenting a core of high  $Z_h$ . In fact, at 10:30 UTC we have report  
33 of heavy rain at Marigliano (40.93°N, 14.46°E) and of hail mixed with rain in Avellino (40.91°N,  
34 14.79°E). Finally, at 10:55 UTC the cell is in its weakening phase.

As pointed out in Section 1, GR may suffer from some limitations in observing convective events that can hamper the use of their measurements. Figure 7, showing the vertical section at 209.5° of the volume collected at 08:45 UTC (time of the GPM-CO overpass) along with a ground profile, explains well these limitations. Limits of the nominal 1° antenna beamwidth and maximum range, different for each elevation angle, are reported. Although the radar site is at a height of 710 m a.s.l., the ground profile shows that orographic reliefs partially shield the lower beam (0.5°). These factors determine that lower layers of the convective cell cannot be observed properly. Top panel highlights the core of reflectivity higher than 55 dBZ, implying the presence of hail or hail mixed with rain, extending above 12 km, that is the maximum height reached by the radar beam. Beyond 120 km, the maximum height of radar beam is 12 km. In addition, for the rays at elevations of 4.5 and 5.5 degrees, the cell extends likely beyond the maximum range of measurements and therefore the ground radar misses part of the hailstorm. A different scanning strategy could have limited this problem. However, a height of 12 km is appropriate for observing most of convection occurring in the region and the scanning strategy was accordingly designed.

The middle panel shows, along with a negative differential reflectivity likely due to the influence of differential attenuation (not corrected), a peak at the border of the cell in correspondence of a dip in  $\rho_{hv}$  (bottom panel) that clearly reveals a three-body scattering (Hubbert and Bringi 2000) pointing out the presence of large hailstones. Nonetheless, an increase of  $Z_{dr}$  at 145 km from the radar up to the height of 5 km reveals the presence of a  $Z_{dr}$  column, a feature pointing out a region of updraft. Observational limitations of GR will be taken into account in Section 3.2.3 where GR  $Z_h$  and  $Z_{dr}$  measurements will be used to support the analysis of GPM-CO measurements in relation to lightning activity.

### ***3.2 GPM observations of the hailstorm mature stage***

In this section we focus on the analysis of the observations from the GPM-CO (GMI and DPR) and from MHS, used in synergy with ground-based polarimetric radar measurements and LINET data, to characterize the storm at its mature stage in terms of its 3-D structure. Finally, GMI and MHS are used to provide observational evidence of the strengths and rarity of this storm at global scale.

#### ***3.2.1 PMW observations: GMI and MHS***

Descending orbit 8630 of GPM-CO captured the hailstorm in its mature stage at 08:47 UTC, when it was approaching the coast of Naples. GMI, DPR-Ku and DPR-Ka swaths cover the deep convective core over the Tyrrhenian Sea, while the anvil, extending out to the Adriatic Sea, is fully



covered by GMI and only partially by DPR (Fig. 8).

Different characteristics of the storm can be analyzed looking at the TBs measured at the different frequencies (Fig. 9). At 18.7 GHz-V -- and less evidently at 18.7 GHz-H (not shown) due to the lower sea surface emissivity at H-polarization --, a “cold” area over the sea (14°E, 41°N) is present, with TBs 60-70 K lower than the surrounding. Such behavior is very rare, as at this frequency storms are usually identified as warm emission signatures over the radiatively-cold sea background, and is due to scattering of the upwelling radiation by high density, large ice particles in the convective core of the storm. At 36.5 GHz (V and H) such scattering effects in the main convective core of the storm off the coast of Naples produce TB depressions (i.e., TB values lower than in the surrounding area) larger than 100 K; in contrast, a secondary cell (13.5°E, 41°N) is evidenced, especially at H-polarization, by TBs 30 K higher than the surroundings, thus indicating presence of precipitation without significant scattering by large graupel particles.

At the high frequency window channels (89 and 166 GHz), the area of TB depressions extends over land, thus including the convective core (with TB depressions as high as 200 K) and part of the very large anvil spreading from the Tyrrhenian Sea to the Adriatic Sea towards the North-East. This latter is more evident at 166 GHz (with TBs ranging between 170 and 200 K) than at 89 GHz because the low-density ice particles (such as snowflakes and aggregates) that are present in the upper cloud layers of the outflow region have higher scattering efficiency at the higher frequency (e.g., Hong 2007, Defer et al., 2014). In contrast, the lowest TBs in the convective core are about 20 K higher at 166 GHz than at 89 GHz. This may be partly due to the fact that emission by water vapor and by supercooled droplets (mostly in the updraft region) is larger at 166 GHz, but is also a clear sign of the presence of large, high-density ice particles. Casella et al. (2008) have shown that for large graupel (or hail) particles, the single scattering efficiency at 150 GHz (and so at 166 GHz) is lower than at 89 GHz, while the asymmetry factor is higher. Finally, note that the main core of the secondary cell observed at 36.5 GHz is also evident at these higher frequencies as a scattering signature (TBs as low as 150 K) over the surrounding radiatively-warm background.

The TB image at  $183.31 \pm 7$  GHz is similar to that at 166 GHz since both channels respond in a quite similar way to ice scattering. On the other hand, comparison with the TB image at  $183.31 \pm 3$  GHz clearly shows that TB depressions at  $183.31 \pm 7$  GHz are usually deeper and extend over a larger area. Generally speaking, this is because of a larger damping of the ice scattering effects by the atmospheric water vapor when frequency is closer to the absorption band center. In other words, since radiation can penetrate deeper into the cloud as the frequency moves away from the absorption band center, at  $183.31 \pm 7$  GHz it is subject to larger scattering from mid and low cloud layers, while at  $183.31 \pm 3$  GHz it is affected by the higher cloud layers only – see Burns et al. (1997)

and Hong et al. (2005) for a thorough explanation of these effects involving the 183 GHz channels.

One of the innovations of GMI with respect to other radiometers in the constellation is the presence of the dual polarization channels at 166 GHz. Fig. 10 shows the TB differences in the vertical and horizontal polarization channels (hereinafter V–H) for both the 89 and 166 GHz frequencies. Noteworthy, these quantities can be directly related to the preferential orientation of the ice hydrometeors in the cloud, including small ice crystals (e.g., Spencer et al., 1989; Defer et al., 2014). In this regard, we note that while the polarization signal V–H at 89 GHz is mostly affected by the precipitating ice particles in the convective region and by the background surface (as the land/sea transition clearly shows), at 166 GHz it depends also on the orientation of the smaller ice particles in the upper cloud layers and in the anvil region (which is the reason why the anvil appears more evident and larger at this frequency).

At both frequencies, the convective core is well identified by V–H values close to 0 K which, in conjunction with the very low TBs discussed above, indicates the presence of large high-density randomly-oriented/tumbling ice particles even in the upper layers of the strong updraft. Nevertheless, we note that the V–H values are always positive (with minima of about 0.5 K and 1.7 K at 89 GHz and 166 GHz, respectively), which may suggest a residual horizontal orientation especially of the smaller ice crystals at the higher levels. [We note that other authors report also negative V–H values explained by the presence of relatively large, mostly vertically oriented non-spherical hydrometeors (e.g., Prigent et al., 2005, Mattos and Machado (2011))]. The convective outflow region corresponds to higher values of V–H associated to the preferential horizontal orientation of non-spherical ice crystals. Here the signal reaches about 9 K and 11 K at 89GHz and 166 GHz, respectively, and shows a rather variable pattern that may reflect the upper cloud physical structure -- i.e., cloud vertical extension, or presence of above anvil plumes affecting the presence and the preferential orientation of small size particles. The large occurrence of the polarized scattering in the anvil of the storm, as well as the magnitude of the polarization, suggests that horizontally oriented oblate particles are very frequent in the cloud ice phase (see also Defer et al., 2014). Finally, for the weaker secondary cell on the north-west corner of the storm, the V–H TB differences are usually somewhat greater than for the convective core, thus indicating that precipitating and non-precipitating ice particles tend to be oriented at all cloud levels (i.e., absence of strong vertical winds). In contrast, the area on the south-east of this cell is characterized by lower V–H values (especially at 89 GHz); if we consider the results of previous Fig. 9 together with the present ones, we can conclude that this area likely corresponds to a portion of the storm of light precipitation, occurring between the back shear anvil of the main cell and the secondary cell.

Fig. 11 shows the TBs measured by the cross-track radiometer MHS during the two overpasses of



the storm at 08:34 UTC (MetOp-A) and 09:28 UTC (MetOp-B) – i.e., just before and after the GMI overpass. While these results provide further evidence of the severity of the storm during its approach to the coast of Naples (as discussed in following Section 3.2.4), here we focus on their comparison with the GMI TBs of Fig. 9. While a quite similar behavior can be found, at least in terms of storm extension and pattern, it is evident that GMI, as compared to MHS, delineates better the structure of the storm because of the higher spatial resolution of its high-frequency channels. For the very same reason, TB depressions are higher for GMI than for MHS. For instance, at 89 GHz the minimum TB for GMI is  $\sim 50$  K lower than for the MetOp-A MHS ( $\sim 70$  K vs.  $\sim 120$  K) – on this regard, we note that this difference should be related to the different IFOV sizes of GMI ( $4.4 \times 7.2$  km<sup>2</sup>) and of MHS [ $34.4 \times 21.4$  km<sup>2</sup>, calculated according to Bennartz (2000)], rather than to the evolution of the storm in the 13-minute time interval between the two overpasses, since SEVIRI images, GR, and LINET data do not show significant differences at the times of the two overpasses.

### 3.2.2 DPR observations

Here we analyze the DPR Ku- and Ka-band measurements and relate them to the GMI TB behavior and to the 3-D structure of the storm. To this end, we consider the three cross-sections of the storm which are indicated in the right panel of previous Fig. 8 – i.e., along-track cross-section “A” (for Ku ray 21 – Ka ray 9) crossing the most intense portion of the storm along the direction of the orbit of the GPM-CO satellite; along-track cross-section “B” (for Ku ray 15 – Ka ray 3) crossing a weaker portion of the storm along the same direction as “A”; and cross-track cross-section “C” (for Ku/Ka scan 4941) crossing the anvil and the storm itself perpendicularly to the GPM-CO orbit.

DPR measurements on the two along-track cross-sections of the storm are shown in Fig. 12 (left and right columns for sections A and B, respectively), together with the corresponding GMI measurements. The effect of the different sensitivity (Toyoshima et al. 2015) and different attenuation at the two radar frequencies is quite evident for both sections. Along cross-section A, the measured (i.e., attenuated) reflectivity  $Z_m$  at Ku band shows a well defined structure of the storm, including the anvil and the main deep convective core. The high values of  $Z_m$  ( $\sim 55$  dBZ at 10 km, 40 dBZ at 14-15 km, and 20 dBZ at 16 km), together with the fact that the subsequent returns from surface are significantly masked in correspondence of the echo top, indicate the presence of a very intense core of high-density ice particles (hail or graupel) in the upper levels which is maintained by a very strong updraft. A mirror echo above 20 km is present in correspondence of the updraft region, where the return signal from the surface is absent (see Li and Nakamura, 2002 for a detailed explanation of this effect). A secondary cell ( $41.1^\circ\text{N}$ ,  $13.6^\circ\text{E}$ ) with  $Z_m \sim 20$  dBZ extending up to 8 km, and a cumulus congestus extending up to 7 km ( $41.8^\circ\text{N}$ ,

1 13.1°E) with  $Z_m$  values as high as 35 dBZ are also evident.

2 The corresponding Ka  $Z_m$  is affected by considerable attenuation below 8 km in the whole  
3 convective region (where surface return is completely masked by attenuation), while the upper level  
4 signal associated to the anvil of the cloud is not visible due to the lower radar sensitivity at this  
5 frequency. Note that in the upper levels of the updraft region  $Z_m$  is lower for Ka- than for Ku-band,  
6 with maximum values around 45 dBZ, because of larger attenuation and multiple scattering  
7 (Battaglia et al., 2015). The behavior of Ku- and Ka-band  $Z_m$  in the region of highest attenuation is  
8 typical of very intense convective cores characterized by large, high-density ice particles and strong  
9 updrafts, and causes the typical “knee” feature of the Ku/Ka Dual Wavelength Ratio (DWR) (not  
10 shown) thoroughly analyzed by Battaglia et al. (2015). If we consider the weaker cross-section B,  
11 we find that Ku  $Z_m$  is not affected by significant attenuation, and shows a weaker structure of the  
12 convective core with values  $\sim 40$  dBZ, associated to precipitation, which is capped by an anvil  
13 having a clear signal at  $\sim 15$  dBZ; in contrast, Ka  $Z_m$  shows significant attenuation in  
14 correspondence of the convective region (with extinction of signal from the surface), while the anvil  
15 is not visible.

16 Let us now consider the TB behavior along the two cross-sections. For cross-section A, the TBs at  
17 the lower frequencies (up to 37 GHz) are mostly affected by the background surface (as evidently  
18 shown by the land/sea transition) except in the deep convective core, where they reach the  
19 minimum values in correspondence of the region of larger attenuation (40.8°N, 13.8°E). On the  
20 other hand, the 89 GHz TBs are much more sensitive to cloud structure: they decrease in  
21 correspondence of the cumulus congestus (41.8°N, 13.1°E) (by 20 K), and then drop in  
22 correspondence of the secondary cell (41.1°N, 13.6°E) (down to 200 K), and, much more, in  
23 correspondence of the deep convective core of the storm, where they reach the minimum value of  
24 69 K because of the already mentioned presence of large graupel/hail particles. Finally, the high-  
25 frequency channels are affected by the presence of the ice particles in the upper layers in different  
26 ways depending on their weighting functions and on cloud structure. For example, while the TBs at  
27 166 GHz and, to a less extent, at  $183.31 \pm 7$  GHz are affected by the scattering from ice even in  
28 correspondence of the cumulus cloud (41.8°N, 13.1°E), the  $183.31 \pm 3$  GHz TBs are sensitive to the  
29 higher cloud layers only. At all high frequencies, the upwelling TBs drop in correspondence of the  
30 secondary cell (with a TB depression which is stronger at 166 GHz than for the water vapor  
31 absorption band) and in the main convective core where they all reach their minimum values, with  
32 TBs at 166 GHz that are 18 K higher than at 89 GHz (as discussed for previous Fig. 9).

33 For the weaker cross-section B, the TBs show a behavior which reflects the presence of the anvil  
34 and of a less intense portion of the storm. While the TBs at the three high frequencies are affected

1 by the presence of the anvil with no precipitation, and gradually decrease going towards the main  
2 convective region, at lower frequencies the upwelling TBs are less affected by the upper cloud  
3 layers and decrease only in presence of precipitation, with the region showing TB depression  
4 getting narrower and weaker as frequency decreases.

5 Along the cross-section C (Fig. 13), moving across the anvil and through the convective core in the  
6 region of minimum TBs, the Ku  $Z_m$  show a slanted vertical structure, which is enhanced by the  
7 effect of the attenuation below 8 km in correspondence of the overshooting top and of the strongest  
8 updraft. The tilted storm is a sign of vertical wind shear and, therefore, of storm severity, and is  
9 associated to the hook-echo evidenced in the analysis of Fig. 6 (08:45 UTC panel). The echo top  
10 height is at 16.25 km in correspondence of the overshooting top, while the forward flank anvil echo-  
11 top height is around 14 km, decreasing in the north-eastern region to 12 km. The TBs reach their  
12 minimum values in correspondence of the overshooting top, with lowest TB at 89 GHz.

### 14 3.2.3 *Lightning activity and MW observations*

15 In this section the electrical activity is analyzed in relation to the cloud vertical development,  
16 updraft strength, and microphysical structure as inferred from the available active and passive MW  
17 observations. The LINET strokes (IC and CG) registered in a 4 min time interval around 08:47  
18 UTC (time of the GPM-CO overpass) are considered. Fig. 14 shows that most of the strokes are  
19 concentrated within the main cell, although some weaker activity, dominated by CG, is present also  
20 in a smaller cell in the West sector of the observed area.

21 The area of minimum TB at 19 GHz (V-polarization) (Fig. 14 upper panel), identifying the presence  
22 of large hailstones or graupel, is in proximity of the region of lightning activity. This happens also  
23 when we look at the Ku-band radar reflectivity (Fig. 14 bottom-left panel), where lightning activity  
24 is mostly located over the area of maximum radar reflectivity. There is also a very good  
25 correspondence in the cloud structure between the DPR and the GR. A hook echo associated to  
26 mesocyclone, very well defined in the GR image (Fig. 14 bottom-right panel), is also noticeable in  
27 Ku-band image (Fig. 14 bottom-left panel). The high Z values around 50 dBZ in the Ku-band and  
28 60 dBZ measured by the C-band radar at 6 km height are clear indications of the presence of hail.  
29 Due to the strong C-band attenuation, the high echo region looks smaller in the GR image.

30 To better understand the relationship between the IC activity and the microphysical properties of the  
31 cloud and to relate the emission height of IC+ and IC- with the storm structure, we have compared  
32 two vertical cross-sections of Ku  $Z_m$  through the major cell and the IC strokes (Fig. 15 top panels).  
33 The strokes found well above the maximum radar cloud top height could actually arise from within

1 the cloud, due to overestimation of IC initiation height (Holler et al., 2009) or could indeed extend  
2 out of the cloud top as “bolt-from-the-blue”, as introduced by Krehbiel et al. (2008). Anyway, most  
3 of the IC strokes are found within the part of the storm’s convective core characterized by the  
4 highest reflectivity, above the melting level, which is around 4.5 km, and on average, the IC+  
5 registered positions are higher than the IC- (as discussed in Section 3.1).

6 The vertical cross-sections of the GR  $Z_h$  along the same directions of DPR (Fig. 15 middle panels)  
7 show a really good agreement with  $Z_m$ , apart from the underestimation of the storm height and  
8 extension along the range direction in the GR observations. In the GR, at lower levels  $Z_h$  can be  
9 attenuated because of partial beam shielding and propagation attenuation, while  $Z_m$  is subjected to  
10 attenuation from the hydrometeors aloft. Propagation attenuation on  $Z_h$  and  $Z_{dr}$  cannot be easily  
11 compensated because of the unavailability of differential phase measurements and because it  
12 presents extinction of return (Tabary et al. 2009). Since  $Z_{dr}$  is not corrected for attenuation,  
13 variations with respect to neighboring areas need to be considered in the analysis instead of absolute  
14  $Z_{dr}$  values.  $Z_h$  values around 60 dBZ are found up to 12-14 km. The analysis of  $Z_{dr}$  vertical cross-  
15 sections (Fig. 15 bottom panels) indicates that the IC+ are mostly located over regions of increased  
16  $Z_{dr}$  aloft, associated to the updraft (already evidenced by the  $Z_{dr}$  column shown in Fig. 7, middle  
17 panel, located at 145 km from radar), while IC- are mostly located in regions of high  $Z_h$  found at the  
18 lower levels, and associated to precipitation.

19 In previous studies peaks of electrical activity have been correlated with cloud vertical  
20 development, as inferred by radar cloud top height and reflectivity at high altitude (e.g., Williams et  
21 al., 1989), and the predominance of CG+ for extended periods of time has been found for severe  
22 thunderstorms producing large hail, and sometimes tornadoes, (e.g., MacGorman and Burgess,  
23 1994; Stolzenburg, 1994; Kennedy et al., 2014 and references therein). Thus the monitoring of CG+  
24 evolution could be useful in the identification of storms with relatively strong, horizontally  
25 extensive updrafts (Lang and Rutledge 2002; Bruning et al. 2012). On the other hand, the results  
26 presented in this section show that also the occurrence of IC+ during the most intense phase of the  
27 Naples hailstorm (shown also in Fig. 5), and their higher emission heights with respect to IC- in the  
28 region of very strong updraft (evident in the left panels of Fig. 15) are associated to the presence of  
29 large hail/graupel. The very strong updraft has three effects: 1) it enhances the riming rate due to  
30 high supercooled liquid water flux (i.e., conditions conducive to the wet growth of hailstones) in the  
31 upper portions of the cloud; 2) it favors the charging mechanisms due to the collisions between ice  
32 crystals and graupel particles (more efficient in presence of supercooled water, e.g., Williams et al.,  
33 1991); 3) it lifts the negative charger to higher altitude in the thundercloud and for longer periods of  
34 time compared to ordinary thunderstorms (12-14 km in our case) [i.e., elevated charge hypothesis,

MacGorman et al. (1989)]. Moreover, when the riming rate is sufficiently enhanced due to high supercooled liquid water flux (i.e., conditions conducive for the wet growth of hailstones), the charging sense can reverse, producing positive charge at mid levels (Saunders 1993), and this might have an impact on the registered IC stroke polarity. The presence of IC+ at lower levels in correspondence of scan 4941 (right panels of Fig. 15) may be associated to the precipitating large hail/graupel.

It is worth noting that the analysis of stroke emission heights from VLF/LF lightning location network such as LINET is strictly linked to the local network configuration (Holler et al., 2009) and on the methodology used for emission height and polarity determination (see for example Wu et al., 2011). Future studies on hail-producing thunderstorms observed by DPR, and occurring in proximity of polarimetric radar, and with the availability of LINET data, will contribute to clarify and investigate further on these interesting and still controversial and debated aspects.

#### *3.2.4 Event characterization at global scale*

Strong TB depressions at low frequencies ( $< 37\text{GHz}$ ) indicate the presence of large ice hydrometeors in the upper portions of clouds, generally associated with strong updrafts. Some specific studies have been carried out in order to find a relationship between minimum TBs at multiple frequencies and hail (e.g., Cecil 2009; Cecil and Blankenship 2012; Leppert and Cecil, 2015; Ferraro et al. 2015). Cecil (2009) compared TRMM TMI TBs at 19, 37, and 85 GHz with hail reports in the U.S. severe-storm database and found that large hail was more likely associated with lower TBs than smaller hail, while hail occurred more often with TBs lower than 70K, 180K and 230K at 85, 37, and 19 GHz, respectively, with the 37 GHz channel being best suited for hail detection from TMI. More recently Leppert and Cecil (2015) carried out a study to determine the signatures of various hydrometeor species in terms of TBs from airborne passive microwave data measured at frequencies between 10 and 183 GHz used by the GMI. Results indicate that hail is associated with an ice-scattering signature at all frequencies examined, with probability of low-level hail increasing for TBs below 240 K at 19 GHz, 170 K at 37 GHz, 80 K at 89.0 GHz, 100 K at 165.5 GHz, and 100 K at  $183.3\pm 7$  GHz.

Table 2 provides the values of the GMI minimum TBs and Polarization Corrected Temperatures (PCTs, Spencer et al., 1989, Kidd 1998) for the hailstorm under study. Evidently, the Naples hailstorm TBs are under the thresholds fixed for hail detection for all examined channels, while showing remarkable low values at low frequencies (including 19 GHz).

The severity of the Naples hailstorm can be evidenced also by the comparison of the minimum

values of MHS TBs (shown in Table 3) and those found for the record hailstorm studied by Ferraro et al. (2015), that produced a 20 cm hailstone. In our case, TB minimum values measured by MetOp-B are comparable with those for the U.S. case study, and even lower if we consider the measurements by MetOp-A.

Ferraro et al. (2015) developed a hail detection algorithm and a climatology of hail occurrence over the continental U.S. using AMSU/MHS data from all operating satellites during 2000–2011 for the months of March to September, providing thresholds for TB values at each frequency channel and the corresponding hail size. TBs measured by both MetOp-A and MetOp-B for the Naples hailstorm are well below the mean TB thresholds indicated by Ferraro et al. (2015) and these values correspond to reports of hailstone size larger than 7.5 cm.

The availability of several years of observations by PMW instruments has allowed to build large databases of Precipitation Features (hereinafter PFs), i.e. contiguous pixels on the basis of some specific criteria (Mohr and Zipser, 1996, Nesbitt et al., 2000, Liu et al., 2008), widely used for several applications (e.g. Cecil et al., 2005; Liu and Zipser, 2005; Zipser et al. 2006). Very recently, a GPM PF database has been developed based on the advanced capabilities of the GPM-CO instruments (Liu and Zipser, 2015) -- see <http://atmos.tamucc.edu/trmm/data/gpm>.

We investigated how rare is the Naples hailstorm at mid-latitudes and globally, by selecting all the PFs with minimum TBs and PCT lower than those found for the Naples hailstorm over a period of 26 months of GPM observations (03/2014-04/2016). The rarity of the Italian case study is clearly evident if we look at the results in Table 4. The storm ranks globally as first, second and fourth for the minimum TBs at 19 GHz (V-pol), 23 GHz and minimum PCT at 37 GHz, respectively. Two of the three events found with PCT at 37 GHz lower than the Naples hailstorm occurred over the CONUS (June 2014, in Nebraska and May 2015 in Oklahoma). Such TB depressions at these frequencies have never been observed in the Mediterranean area. Also the minimum TB values found at higher frequencies are very rarely found in the Mediterranean area (the Naples hailstorm ranks as third, sixth and fourth considering the minimum TB at 89, 166 and  $183\pm3$  GHz respectively). The strong TB depressions at low frequencies (noteworthy at 19 GHz) found for the Naples hailstorm are linked to the microphysical structure of the large convective core of the storm, characterized by a very strong updraft sustaining large massive ice particles at the upper levels, as inferred from the analysis carried out in the previous sections (we have verified that the low sea surface emissivity has a negligible impact on the TBs in the convective core).

#### **4. Summary and conclusions**



1 In this paper we use all available ground- and space-based observations to document an  
2 exceptionally severe hailstorm which occurred in central Mediterranean on 5 September, 2015, and  
3 illustrate the unprecedented capabilities of the GPM-CO satellite for characterizing the structure of  
4 this kind of storms. Specifically, the study is based on the use of GMI and DPR measurements  
5 taken by GPM-CO during the overpass that captured the storm in its mature stage, when the main  
6 convective core was approaching the coast of Naples, in parallel with MSG SEVIRI IR  
7 observations, LINET strokes data, and ground-based C-band radar polarimetric measurements.

8 The mesoscale storm under study developed off shore and moved inland in its mature phase. It  
9 consisted of a supercell followed by secondary cells, and dropped 7-10 cm sized hailstones along its  
10 path over the sea and over land. The supercell structure is clearly revealed by the presence of cloud  
11 top plumes observed by MSG SEVIRI and of a strong hook-echo in the C-band polarimetric  
12 ground radar measurements.

13 The maximum stroke rate was around  $300 \text{ min}^{-1}$  and we have found that the lightning initiation was  
14 temporally related to the maximum vertical mass transport computed using MSG SEVIRI IR data.  
15 A total of 20846 LINET strokes were registered in two hours (07:00-09:00 UTC) during the most  
16 intense phase of the storm. The time series of positive and negative IC and CG strokes provides an  
17 indication of the variable electrical structure of the storm, which was characterized by an increased  
18 IC+ fraction and emission height during its most intense phases and by the highest IC+ stroke rates  
19 when very large hailstones were reported at the surface. Moreover, we estimate by means of MSG  
20 SEVIRI analyses that the maximum cooling rate at cloud top was around  $4.5 \text{ K min}^{-1}$  in the growth  
21 phase (with a cloud top minimum temperature of 198 K) and that the peak updraft speed was  
22 compatible with 8-10 cm sized hailstones at the ground.

23 We show that the available GPM measurements (especially by GMI and DPR onboard GPM-CO,  
24 but also by the MHS PMW radiometers onboard MetOp-A and MetOp-B) integrate the  
25 observations summarized above, and help overcoming many of the limitations suffered by ground  
26 based instruments and VIS-IR sensors on geosynchronous satellites. Specifically, GMI  
27 measurements provide useful information on the different nature of the ice hydrometeors in the  
28 outflow region (low-density ice hydrometeors such as snowflakes and aggregates) and in the  
29 convective core (graupel or hail), while delineating well the structure of the storm because of their  
30 higher spatial resolution with respect to the other PMW radiometers of the GPM constellation. In  
31 particular, the fact that the convective core of the storm shows a deep GMI TB depression at 19  
32 GHz and that the minimum TBs at 166 GHz are 20 K higher than at 89 GHz are a clear indication  
33 of the presence of large, high-density ice particles at different levels of the updraft region. Finally,  
34 the newly available 166 GHz polarization differences show patterns indicating a complex physical

1 structure and different hydrometeor characteristics in the upper cloud layers: randomly  
2 oriented/tumbling ice particles brought to the upper levels by the strong updraft in the convective  
3 core, and non-spherical ice crystals with preferential horizontal orientation in the convective  
4 outflow region (likely horizontally oriented oblate ice particles).

5 GPM measurements are also useful to classify the severity of the Naples storm at global scale. We  
6 find that the storm was exceptionally intense since it was characterized by the deepest 19V GHz TB  
7 depression (158 K) over a 26-month period of GMI global observation, and since it shared  
8 extremely low TBs (and PCTs) records at 23 and 37 GHz with two storms in the CONUS, and also  
9 with tropical storms at higher frequencies. MetOp-A and MetOp-B MHS measurements confirm  
10 these findings because of the extremely low TBs as compared to a 12-year MHS hailstorm  
11 climatology over the U.S., which are compatible with hailstone size larger than 7.5 cm. DPR  
12 measurements provide further support to the previous GMI analyses and findings, while  
13 highlighting the slanted structure of the main updraft and its vertical structure, and measuring the  
14 overshooting top height at 16.25 km a.s.l., with the presence of large ice particles in highest cloud  
15 layers (i.e.  $Z \geq 45$  dBZ at 14 km a.s.l.). The vertical distribution of IC lightning according to their  
16 polarity and to vertical DPR reflectivity (and ground-radar differential reflectivity) reveals that the  
17 complex multi-polar electrical structure of the storm was connected to the presence of a very strong  
18 updraft (with more IC+ at higher levels than IC-, while in other regions of the storm the IC polarity  
19 distribution changes). Note that similar, or even more distinct, IC polarity distribution was evident  
20 during other phases of the storm evolution -- e.g., at the time of reports of large hail at the surface.  
21 Nevertheless, we point out that in order to establish if the observed IC distribution is a further  
22 evidence of the severity of the Naples hailstorm, or if it is typical of severe storms producing large  
23 hail, further studies and observational datasets are necessary.

24 In essence, this paper shows that the unique spaceborne measurements available from GPM-CO  
25 provide observational evidence of extremely rare features of the Naples hailstorm, and, in  
26 combination with more established observational data, contribute towards our understanding of  
27 such severe and rapidly evolving convective systems. In this regard, it is worth noting that  
28 operational and research Numerical Weather Prediction (NWP) models completely missed the  
29 forecast of this storm, thus fostering deeper research to increase knowledge of these events which  
30 often severely impact ground structures and human activities. The extremely rapid development  
31 over the sea (with no orographic forcing) of such localized and intense convective systems, together  
32 with the fact that often the local forcing is not represented in the data used as initial conditions in an  
33 operational setting, poses great challenges to a correct simulation of the dynamical and  
34 microphysical processes leading to their development. Nevertheless, we leave to future and



dedicated studies the investigation of the mechanisms that have lead to the development and evolution of such exceptional hailstorm, as well as the quantitative retrieval of the storm microphysical structure using the GPM-CO GMI and DPR measurements (accounting for attenuation correction and multiple scattering). We anticipate that to this end, it will be necessary to combine cloud-resolving model and radiative transfer simulations with the observational dataset that has been analyzed in the present paper.

Finally, this observational study indicates that the quantitative exploitation of the unprecedented tools available from GPM should be oriented not only to the retrieval of precipitation rates, but also to the understanding of cloud structure and dynamics of extreme events which periodically devastate the Mediterranean coastal regions; moreover, the use of GPM data would help assessing climate change signatures in the Mediterranean area, where such severe events are becoming more and more frequent, while the available observation networks based only on raingauge and weather radar are unlikely to provide measurements with the needed space cover, detail and accuracy.

## Acknowledgements

This research was supported by the Earth2Observe “Global Earth Observation for Integrated Water Resource Assessment” project funded under the EU DG Research 7th Framework Programme (FP7), and by EUMETSAT through the project “Satellite Application Facility on Support to Operational Hydrology and Water Management” (H-SAF). The authors are very grateful to Dr. Iguchi (from JAXA) for providing information on the V04 2A-DPR product, and to the Precipitation Measuring Mission Science Team for collaborative and fruitful discussions on some of the topics presented in this article. The authors would like to acknowledge the Civil Protection Department of Italy for providing ground-based radar data, JAXA and NASA data processing team for providing the GPM data, and EUMETSAT for providing MSG data. V04-GPM data were downloaded from the Precipitation Processing System (<ftp://arthurhou.pps.eosdis.nasa.gov/>): DOI 10.5067/GPM/DPR/DPR/2A for the 2A-DPR, 10.5067/GPM/GMI/R/1C/04 for the 1C-R-GMI, 10.5067/GPM/MHS/METOPA/1C/04 and 10.5067/GPM/MHS/METOPB/1C/04 for the 1C-MHS. MSG SEVIRI RSS data were downloaded from the EUMETSAT Earth Observation Portal. LINET data have been provided by Nowcast GmhB (<https://www.nowcast.de/>) within a scientific agreement between Prof. H.-D. Betz and the Satellite Meteorology Group of CNR-ISAC in Rome.

## References

- Adler, R. F., and D. D. Fenn, 1979: Thunderstorm intensity as determined from satellite data. *J. Appl. Meteorol.*, 18, 502–517.
- Battaglia, A., S. Tanelli, K. Mroz, and F. Tridon, 2015: Multiple scattering in observations of the GPM dual-frequency precipitation radar: Evidence and impact on retrievals, *J. Geophys. Res.: Atmos.*, 120, 4090–4101, doi:10.1002/2014JD022866, 2015.
- Bartzokas, A., Azzopardi, J., Bertotti, L., Buzzi, A., Cavaleri, L., Conte, D., Davolio, S., Dietrich, S., Drago, A., Drofa, O., Gkikas, A., Kotroni, V., Lagouvardos, K., Lolis, C.J., Michaelides, S., Miglietta, M., Mugnai, A., Music, S., Nikolaidis, K., Porcú, F., Savvidou, K., Tsirogianni, M.I., 2010, The RISKMED project: Philosophy, methods and products, *Nat. Hazards Earth Syst. Sci.*, 10, 1393–1401.
- Bech, J., J. Arús, S. Castán, N. Pineda, T. Rigo, J. Montanyà, O. van der Velde, 2015: A study of the 21 March 2012 tornadic quasi linear convective system in Catalonia, *Atmos. Res.*, 158, 192–209, DOI: 10.1016/j.atmosres.2014.08.009.
- Bennartz, R., 2000: Optimal convolution of AMSU-B to AMSU-A. *J. Atmos. Oceanic Technol.*, 17, 1215–1225.
- Betz, H.-D., K. Schmidt, P. Oettinger, and M. Wirz, 2004: Lightning detection with 3-D discrimination of intracloud and cloud-to-ground discharges, *Geophys. Res. Lett.*, 31, L11108, doi:10.1029/2004GL019821.
- Betz, H.-D., K. Schmidt, P. Laroche, P. Blanchet, W. P. Oettinger, E. Defer, Z. Dziewit, and J. Konarski, 2009: LINET – An international lightning detection network in Europe. *Atmos. Res.*, 91, 564–573, doi:10.1016/j.atmosres.2008.06.012, 2009.
- Brook, M., and N. Kitagawa, 1960: Some aspects of lightning activity and related meteorological conditions, *J. Geophys. Res.*, 65, 1203–1210, 1960.
- Bruning, E. C., S. A. Weiss, and K. M. Calhoun, 2012: Continuous variability in thunderstorm primary electrification and an evaluation of inverted-polarity terminology. *Atmos. Res.*, 135–136, 274–284, doi:10.1016/j.atmosres.2012.10.009.
- Buzzi, A., S. Davolio, P. Malguzzi, O. Drofa, and D. Mastrangelo, 2014: Heavy rainfall episodes over Liguria in autumn 2011: numerical forecasting experiments. *Nat. Hazards Earth Syst. Sci.*, 14, 1325–1340.
- Burns B. A., X. Wu, and G. R. Diak, 1997: Effects of Precipitation and Cloud Ice on Brightness Temperatures in AMSU Moisture Channels, *IEEE Trans. Geosci. Remote Sens.*, 35, 1429–1437.
- Casella, D., A. Mugnai, P. Sanò, and M. Formenton, 2008: Microwave single-scattering properties of randomly oriented soft-ice hydrometeors. *Adv. Geosci.*, 17, 79–85.
- Cassola, F., F. Ferrari, A. Mazzino, 2015: Numerical simulations of Mediterranean heavy precipitation events with the WRF model: A verification exercise using different approaches. *Atmos. Res.*, 164–165, 210–225.
- Cavicchia, L., H. von Storch, S. Gualdi, 2014: A long-term climatology of medicanes. *Climate Dyn.* 43, 1183–1195.
- Cecil, D. J., S. J. Goodman, D. J. Boccippio, E. J. Zipser, and S. W. Nesbitt, 2005: Three years of TRMM precipitation features. Part I: Radar, radiometric, and lightning characteristics. *Mon. Wea. Rev.*, 133, 543–566.
- Cecil, D. J., 2009: Passive microwave brightness temperatures as proxies for hailstorms. *J. Appl. Meteorol. Climatol.*, 48, 1281–1286, doi:10.1175/2009JAMC2125.1.
- Cecil, D. J., and C. B. Blankenship, 2012: Toward a global climatology of severe hailstorms as

estimated by satellite passive microwave imagers. *J. Climate*, 25, 687–703, doi:10.1175/JCLI-D-11-00130.1.

Cohuet, J.B., R. Romero, V. Homar, V. Ducrocq, and C. Ramis, 2011: Initiation of a severe thunderstorm over the Mediterranean Sea. *Atmos. Res.*, 100, 603–620.

Defer, E., V. S. Galligani, C. Prigent, and C. Jimenez, 2014: First observations of polarized scattering over ice clouds at close-to-millimeter wavelengths (157 GHz) with MADRAS on board the Megha-Tropiques mission. *J. Geophys. Res.: Atmos.*, 119, 12301–12316, doi:10.1002/2014JD022353.

Di Paola F., E. Ricciardelli, D. Cimini, F. Romano, M. Viggiano, V. Cuomo, 2014: Analysis of Catania flash flood case study by using combined microwave and infrared technique. *J Hydrometeor.*, 15, 1989–1998.

Drobinski, P., Ducrocq, V., Alpert, P., Anagnostou, E., Béranger, K., Borga, M., Braud, I., Chanzy, A., Davolio, S., Delrieu, G., Estournel, C., Filali Boubrahmi, N., Font, J., Grubišić, V., Gualdi, S., Homar, V., Ivančan-Picek, B., Kottmeier, C., Kotroni, V., Lagouvardos, K., Lionello, P., Llasat, M.C., Ludwig, W., Lutoff, C., Mariotti, A., Richard, E., Romero, R., Rotunno, R., Roussot, O., Ruin, I., Somot, S., Taupier-Letage, I., Tintor, J., Uijlenhoet, R., Wernli, H., 2014, HYMEX: A 10-year multidisciplinary program on the mediterranean water cycle. *Bull. Amer. Meteorol. Soc.*, 95, 1063-1082.

Emanuel, K., 2005. Genesis and maintenance of “Mediterranean hurricanes”. *Adv. Geosci.* 2, 217-220.

Ferraro, R., J. Beauchamp, D. Cecil, and G. Heymsfield, 2015: A prototype hail detection algorithm and hail climatology developed with the Advanced Microwave Sounding Unit (AMSU). *Atmos. Res.*, 163, 24-35, doi:10.1016/j.atmosres.2014.08.010.

Ferretti, R., Pichelli, E., Gentile, S., Maiello, I., Cimini, D., Davolio, S., Miglietta, M. M., Panegrossi, G., Baldini, L., Pasi, F., Marzano, F. S., Zinzi, A., Mariani, S., Casaioli, M., Bartolini, G., Loglisci, N., Montani, A., Marsigli, C., Manzato, A., Pucillo, A., Ferrario, M. E., Colaiuda, V., and Rotunno, R.: Overview of the first HyMeX Special Observation Period over Italy: observations and model results, *Hydrol. Earth Syst. Sci.*, 18, 1953-1977, doi:10.5194/hess-18-1953-2014, 2014.

Flaounas, E., K. Lagouvardos, V. Kotroni, C. Claud, J. Delanoë, C. Flamant, E. Madonna, and H. Wernli, 2015: Processes leading to heavy precipitation associated with two Mediterranean cyclones observed during the HyMeX SOP1. *Quart.J.Roy. Meteorol. Soc.* doi: 10.1002/qj.2618

Formenton, M., G. Panegrossi, D. Casella, S. Dietrich, A. Mugnai, P. Sanò, F. Di Paola, H.-D. Betz, C. Price, and Y. Yair, 2013: Using a cloud electrification model to study relationships between lightning activity and cloud microphysical structure. *Nat. Hazards Earth Syst. Sci.*, 13, 1085-1104.

Friedrich, K., U. Germann, J. J. Gourley, and P. Tabary, 2007: Effects of radar beam shielding on rainfall estimation for the polarimetric C-band radar. *J. Atmos. Oceanic Technol.* 24, 1839–1859, doi: 10.1175/JTECH2085.1.

Giorgi, F., 2006: Climate change hot-spots. *Geophys. Res. Lett.*, 33, L08707, doi:10.1029/2006GL025734.

Höller, H., H.-D. Betz, K. Schmidt, R.V. Calheiros, P. May, E. Houngrinou, G. Scialom, 2009: Lightning characteristics observed by a VLF/LF lightning detection network (LINET) in Brazil, Australia, Africa and Germany. *Atmos. Chem. Phys.*, 9, 7795–7824.

Hong, G., G. Heygster, J. Miao, and K. Kunzl, 2005: Detection of tropical deep convective clouds from AMSU-B water vapor channels measurements. *J. Geophys. Res.*, 110, D05205, doi:10.1029/2004JD004949.

Hong, G., 2007: Parameterization of scattering and absorption properties of nonspherical ice crystals at microwave frequencies. *J. Geophys. Res.*, 112, D11208, doi:10.1029/2006JD008364.

1 Hou, A. Y., R. K. Kakar, S. Neeck, A. a. Azarbarzin, C. D. Kummerow, M. Kojima, R. Oki, K.  
2 Nakamura, and T. Iguchi, 2014: The Global Precipitation Measurement (GPM) Mission. *Bull.*  
3 *Amer. Meteorol. Soc.*, 95, 701–722, doi:10.1175/BAMS-D-13-00164.1

4 Houze, R. A., W. Schmid, R.G. Fovell, H. H. Schiesser, 1993: Hailstorms in Switzerland: left  
5 movers, right movers, and false hooks, *Mon. Wea. Rev.*, 121, 3345–3370

6 Hubbert J. C. and V. N. Bringi, 2000: The Effects of Three-Body Scattering on Differential  
7 Reflectivity Signatures. *J. Atmos. Oceanic Technol.* 17, 51–61.

8 Jansa, A., Alpert, P., Arbogast, P., Buzzi, A., Ivancan-Picek, B., Kotroni, V., Llasat, M.C., Ramis,  
9 C., Richard, E., Romero, R., Speranza, A., 2014, MEDEX: A general overview, *Nat. Hazards Earth*  
10 *Syst. Sci.*, 14, 1965-1984.

11 Jiang, H., C. Liu, and E. J. Zipser, 2011: A TRMM-based tropical cyclone cloud and precipitation  
12 feature database. *J. Appl. Meteor. Climatol.*, 50, 1255–1274

13 Kennedy, P. C., S. A. Rutledge, B. Dolan, and E. Thaler, 2014: Observations of the 14 July 2011  
14 Fort Collins Hailstorm: Implications for WSR-88D-Based Hail Detection and Warnings. *Wea.*  
15 *Forecasting*, 29, 623-638, DOI: 10.1175/WAF-D-13-00075.1

16 Kidd, C., 1998: On rainfall retrieval using polarization-corrected temperatures. *Int. J. Remote Sens.*,  
17 19, 981-996, doi: 10.1080/014311698215829.

18 Kotroni, V, K. Lagouvardos, E. Defer, S. Dietrich, F. Porcù, C. M. Medaglia, M. Demirtas, 2006:  
19 The Antalya 5 December 2002 storm: observations and model analysis. *J. Appl. Meteorol.*, 45, 576-  
20 590.

21 Krehbiel, P. R., J. A. Rioussel, V. P. Pasko, R. J. Thomas, W. Rison, M. A. Stanley, and H. E.  
22 Edens, 2008: Upward electrical discharges from thunderstorms. *Nature Geosci.*, 1, 233–237.

23 Kulie, M. S., and Bennartz, R.: Utilizing Spaceborne Radars to Retrieve Dry Snowfall, *J. Appl.*  
24 *Meteorol. Clim.*, 48, 2564–2580, 2009

25 Kummerow C., W. Olson, and L. Giglio, 1996: A simplified scheme for obtaining precipitation and  
26 vertical hydrometeor profiles from passive microwave sensors, *IEEE Trans. Geosci. Remote Sens.*,  
27 34, 1213-1232.

28 Kummerow C., J. Simpson, O. Thiele, W. Barnes, A. T. C. Chang, E. Stocker, R. F. Adler, A. Hou,  
29 R. Kakar, F. Wentz, P. Ashcroft, T. Kozu, Y. Hong, K. Okamoto, T. Iguchi, H. Kuroiwa, E. Im, Z.  
30 Haddad, G. Huffman, B. Ferrier, W. S. Olson, E. Zipser, E. A. Smith, T. T. Wilheit, G. North, T.  
31 Krishnamurti, and K. Nakamura, 2000: The status of the Tropical Rainfall Measuring Mission  
32 (TRMM) after two years in orbit, *J. Appl. Meteorol.*, 39, 1965-1982, 2000.

33 Lang, T.J., and S.A. Rutledge, 2002: Relationships between convective storm kinematics,  
34 precipitation, and lightning, *Mon. Wea. Rev.*, 130, 2492-2506.

35 Llasat, M. C., M. Llasat-Botija,, O. Petrucci, A. A. Pasqua, J. Rosselló, F. Vinet, and L. Boissier,  
36 2013: Towards a database on societal impact of Mediterranean floods within the framework of the  
37 HYMEX project. *Nat. Hazards Earth Syst. Sci.*, 13, 1337–1350.

38 Leppert II, K.D., D.J. Cecil, 2015: Signatures of hydrometeor species from airborne passive  
39 microwave data for frequencies 10-183 GHz. *J. Appl. Meteorol. Climatol.*, 54, 1313–1334, doi:  
40 <http://dx.doi.org/10.1175/JAMC-D-14-0145.1>.

41 Levizzani, V. and M. Setvak, 1996: Multispectral, High-Resolution Satellite Observations of  
42 Plumes on Top of Convective Storms. *J. Atmos. Sci.*, 53, 361-369.

43 Levizzani, V., Bauer, P., Turk, F.J. (Eds.), 2007. *Measuring Precipitation from Space:*  
44 *EURAINSAT and the Future*, Springer, Dordrecht, The Netherlands, 748 pp., ISBN: 1-4020-5834-  
45 9.

1 Lee Y-K, T.J. Greenwald, P. Yang, S. Ackerman and H.-L. Huang, 2010, Global distribution of  
2 instantaneous daytime radiative effects of high thin clouds observed by the cloud profiling radar, *J.*  
3 *Appl. Remote Sens.* 4(1), 043543.

4 Li, J. and K. Nakamura, 2002: Characteristics of the mirror image of precipitation observed by the  
5 TRMM Precipitation Radar. *J. Atmos. Oceanic Technol.* 19, 145–158.

6 Liu, C., and E. Zipser (2005), Global distribution of convection penetrating the tropical tropopause,  
7 *J. Geophys. Res.*, 110, D23210, doi:10.1029/2005JD00006063.

8 Liu, C., E. J. Zipser, D. J. Cecil, S. W. Nesbitt, and S. Sherwood, 2008: A cloud and precipitation  
9 feature database from 9 years of TRMM observations. *J. Appl. Meteorol. Climatol.*, 47, 2712–2728,  
10 doi:10.1175/2008JAMC1890.1

11 Liu, C., and E. Zipser, 2005: Global distribution of convection penetrating the tropical tropopause.  
12 *J. Geophys. Res.*, 110, D23210, doi:10.1029/2005JD00006063.

13 Liu, C., E. J. Zipser, D. J. Cecil, S. W. Nesbitt, and S. Sherwood, 2008: A cloud and precipitation  
14 feature database from 9 years of TRMM observations. *J. Appl. Meteorol. Climatol.*, 47, 2712–2728,  
15 doi:10.1175/2008JAMC1890.1.

16 Liu, C., and E. J. Zipser, 2015: The global distribution of largest, deepest, and most intense  
17 precipitation systems. *Geophys. Res. Lett.*, 42, doi:10.1002/2015GL063776.

18 MacGorman , D. R., V. Mazur, W. D. Rust, W. L. Taylor, and B. C. Johnson, 1989: Lightning rates  
19 relative to tornadic storm evolution on 22 May 1981. *J. Atmos. Sci.*, **46**, 221–250.

20 MacGorman D. R., and D. W. Burgess, 1994: Positive cloud-to-ground lightning in tornadic storms  
21 and hailstorms. *Mon. Wea. Rev.*, 122, 1671– 1697.

22 Manzato, A., S. Davolio, M. M. Miglietta, A. Pucillo, and M. Setvák, 2014: 12 September 2012: A  
23 supercell outbreak in NE Italy?. *Atmos. Res.*, 153, 98–118.

24 Mattos, E.V., Machado, L.A.T., 2011. Cloud-to-ground lightning and Mesoscale Convective  
25 Systems. *Atmos. Res.* 99 (3-4), 377–390. <http://dx.doi.org/10.1016/j.atmosres.2010.11.007>.

26 Mecikalski, J. R., W. M. MacKenzie Jr., M. König, and S. Muller, 2010: Cloud top properties of  
27 growing cumulus prior to convective initiation as measured by Meteosat Second Generation. Part I:  
28 Infrared fields, *J. Appl. Meteorol. Climatol.*, 49, 521–534.

29 Mecikalski, J. R., W. M. Mackenzie, M. Koenig, and S. Muller, 2010b: Use of Meteosat Second  
30 Generation infrared data in 0-1 hour convective initiation nowcasting. Part 2. Use of visible  
31 reflectance. *J. Appl. Meteor. Climat.* 49, 2544–2558.

32 Melani, S., E. Cattani, V. Levizzani, M. Cervino, F. Torricella, M. J. Costa, 2003: Radiative effects  
33 of simulated cirrus clouds on top of a deep convective storm in METEOSAT second generation  
34 SEVIRI channels, *Meteorol. Atmos. Phys.*, 83 doi:10.1007/s00703-002-0554-x

35 Miglietta, M. M., S. Laviola, A. Malvaldi, D. Conte, V. Levizzani, and C. Price, 2013: Analysis of  
36 tropical-like cyclones over the Mediterranean Sea through a combined modelling and satellite  
37 approach. *Geophys. Res. Lett.*, 40, 2400–2405.

38 Mohr, K. I., and E. J. Zipser, 1996: Defining mesoscale convective systems by their ice scattering  
39 signature. *Bull. Amer. Meteorol. Soc.*, 77, 1179–1189.

40 Mugnai, A., Cooper, H.J., Smith, E.A., Tripoli, G.J., 1990. Simulation of microwave brightness  
41 temperatures of an evolving hail storm at SSM/I frequencies. *Bull. Amer. Meteor. Soc.* 71, 2-13

42 Nakajima, T. and T. Nakajima, 1995: Wide-area determination of cloud microphysical properties  
43 from NOAA AVHRR measurements for FIRE and ASTEX regions. *J. Atmos. Sci.*, 52, 4043–4059.

44 Nesbitt, S. W., E. J. Zipser, and D. J. Cecil, 2000: A census of precipitation features in the tropics



using TRMM: Radar, ice scattering, and lightning observations. *J. Climate*, 13, 4087–4106.

Panegrossi G., S. Dietrich, F. S. Marzano, Mugnai, A., E. A. Smith, X. Xiang, G. Tripoli, P. Wang, P. J.P.V. Pojares Baptista, 1998: Use of cloud model microphysics for passive microwave based precipitation retrieval: significance of consistency between model and measurement manifolds, *J. Atmos. Sci.*, 55(9), 1644-1673.

Panegrossi G., D. Casella, S. Dietrich, A. C. Marra, M. Petracca, P. Sanò, A. Mugnai, L. Baldini, N. Roberto, E. Adirosi, R. Cremonini, R. Bechini, G. Vulpiani, and F. Porcù, 2016: Use of the GPM constellation for monitoring heavy precipitation events over the Mediterranean region. *IEEE J. Selected Topics in Appl. Earth Obs. and Rem. Sensing (JSTARS)*, 9, 2733 - 2753, DOI: 10.1109/JSTARS.2016.2520660.

Porcù F., C. Caracciolo, and F. Prodi, 2003: Cloud systems leading to flood events in Europe: A short term climatology. *Meteorol. Appl.*, 10, 217–227.

Porcù, F., A. Carrassi, C.M. Medaglia, F. Prodi and A. Mugnai, 2007: A study on cut-off low vertical structure and precipitation in the Mediterranean region. *Meteorol. Atmos. Phys.*, 96, 121-140.

Price, C., Y. Yair, A. Mugnai, K. Lagouvardos, M.C. Llasat, S. Michaelides, U. Dayan, S. Dietrich, E. Galanti, L. Garrote, N. Harats, D. Katsanos, M. Kohn, V. Kotroni, M. Llasat-Botija, B. Lynn, L. Mediero, E. Morin, K. Nicolaides, S. Rozalis, K. Savvidou, B. Ziv, 2011, The FLASH Project: using lightning data to better understand and predict flash floods, *Environmental Science & Policy*, 14, 898-911.

Prigent, C., Defer, E., Pardo, J.R., Pearl, C., Rossow, W.B., Pinty, J.P., 2005. Relations of polarized scattering signatures observed by the TRMM Microwave instrument with electrical processes in cloud systems. *Geophys. Res. Lett.* 32, L04810. doi:10.1029/2004GL022225.

Reale, O., Atlas, R., 2001. Tropical cyclone-like vortices in the extratropics: Observational evidence and synoptic analysis. *Wea. Forecasting* 16, 7-34.

Roberto, N., E. Adirosi, , L. Baldini, D. Casella, S. Dietrich, P. Gatlin, G. Panegrossi, M. Petracca, P. Sanò, and A. Tokay, 2016: Multi-sensor analysis of convective activity in central Italy during the HyMeX SOP 1.1. *Atmos. Meas. Tech.*, 9, 535-552, doi:10.5194/amt-9-535-2016.

Romero, R., C. Ramis, and V. Homar, 2015: On the severe convective storm of 29 October 2013 in the Balearic Islands: observational and numerical study. *Quart.J.Roy. Meteorol. Soc.*, 141, 1208–1222.

Rosenfeld, D. and I. M. Lenski, 1998: Satellite-based insights into precipitation formation processes in continental maritime convective clouds, *Bull. Amer. Meteorol. Soc.*, 79, 2437-2476

Saunders, C. P. R., 1993: A review of thunderstorm electrification process, *J. Appl. Meteorol.*, 22, 642-655.

Schmetz, J., P. Pili, S. Tjemkes, D. Just, J. Kerkmann, S. Rota, A. Ratier, 2002: An introduction to Meteosat Second Generation (MSG). *Bull. Amer. Meteorol. Soc.*, 83, 977–992.

Schultz, C. J., W. A. Petersen, and L. D. Carey, 2011: Lightning and severe weather: A comparison between total and cloud-to-ground lightning trends. *Wea. Forecasting*, 26, 744–755.

Setvák, M., Rabin, R.M., Wang, P.K., 2007. Contribution of the MODIS instrument to observations of deep convective storms and stratospheric moisture detection in GOES and MSG imagery. *Atmos. Res.* 83, 505–518.

Sikdar, D. N., V. E. Suomi, and C. E. Anderson, 1970: Convective transport of mass and energy in severe storms over the USA. An estimate from a geostationary altitude. *Tellus*, 22, 6, 521-532.

Silvestro, F., N. Reborá, F. Giannoni, A. Cavallo, and L. Ferraris, 2015: The flash flood of the

- 1 Bisagno Creek on 9th October 2014: An ‘unfortunate’ combination of spatial and temporal scales. *J.*
- 2 *Hydrol.*, <http://dx.doi.org/10.1016/j.jhydrol.2015.08.004>.
- 3 Smith, E.A., Kummerow, C., Mugnai, A., 1994. The emergence of inversion-type profile
- 4 algorithms for estimation of precipitation from satellite passive microwave measurements. *Remote*
- 5 *Sens. Rev.* 11, 211-242.
- 6 Spencer, R. W., H. M., Goodman, and R. E., Hood, 1989: Precipitation retrieval over land and
- 7 ocean with the SSM/I: Identification and characteristics of the scattering signal. *J. Atmos. Oceanic*
- 8 *Technol.*, 6, 254-273.
- 9 Stephens, G. L., Vane, D. G., Tanelli, S., Im, E., Durden, S., Rokey, M., Reinke, D., Partain, P.,
- 10 Mace, G. G., Austin, R., L’Ecuyer, T., Haynes, J., Lebsock M., Suzuki, K., Waliser, D., Wu, D.,
- 11 Kay, J., Gettelman, A., Wang, Z., and Marchand, R.: CloudSat mission: Performance and early
- 12 science after the first year of operation, *J. Geophys. Res.*, 113, doi:10.1029/2008JD009982, 2008.
- 13 Stolzenburg, M., 1994: Observations of high ground flash densities of positive lightning in
- 14 summertime thunderstorms. *Mon. Wea. Rev.*, 122, 1740–1750.
- 15 Tabary, P., G. Vulpiani, J. Gourley, R. Thompson, and O. Bousquet, 2009: Unusually high
- 16 differential attenuation at C band: Results from a two-year analysis of the French Trappes
- 17 polarimetric radar data. *J. Appl. Meteorol. Climatol.*, 48, 2037–2053.
- 18 Toyoshima, K., H. Masunaga, and F. A. Furuzawa, 2015: Early evaluation of Ku- and Ka-band
- 19 sensitivities for the Global Precipitation Measurement (GPM) Dual-Frequency Precipitation Radar
- 20 (DPR). *SOLA*, 11, 14–17, doi:10.2151/sola.2015-004.
- 21 Tripoli, G.J., Medaglia, C.M., Dietrich, S., Mugnai, A., Panegrossi, G., Pinori, S., Smith, E.A.,
- 22 2005: The 9-10 November 2001 Algerian flood: A numerical study. *Bull. Amer. Meteorol. Soc.*
- 23 86, 1229-1235.
- 24 Vulpiani, G., Baldini, L., and Roberto, N.: Characterization of Mediterranean hail-bearing storms
- 25 using an operational polarimetric X-band radar, *Atmos. Meas. Tech.*, 8, 4681-4698,
- 26 doi:10.5194/amt-8-4681-2015, 2015.
- 27 Williams, E. R., M. E. Weber, and R. E. Orville, 1989: The relationship between lightning type and
- 28 convective state of thunderclouds, *J. Geophys. Res.*, 94, 13213-13220.
- 29 Williams, E. R., R. Zhang, and J. Rydcok, 1991: Mixed-phase microphysics and cloud
- 30 electrification. *J. Atmos. Sci.*, 48, 2195–2203.
- 31 Wu, T., W. Dong, Y. Zhang, and T. Wang (2011), Comparison of positive and negative compact
- 32 intracloud discharges, *J. Geophys. Res.*, 116, D03111, doi:10.1029/2010JD015233.
- 33 Zipser, E., C. Liu, D. Cecil, S. W. Nesbitt, and S. Yorty, 2006: Where are the most intense
- 34 thunderstorms on Earth?. *Bull. Amer. Meteorol. Soc.*, 87, 1057–1071.

## List of Tables

**Table 1**

Number and rate of strokes in 1 hour-intervals registered by the LINET network over the area swept by the hailstorm from the lightning initiation (LI) at 06:12 UTC until 11:00 UTC.

| Time (UTC)            | 06:12-07:00 | 07:00-08:00 | 08:00-09:00 | 09:00-10:00 | 10:00-11:00 |
|-----------------------|-------------|-------------|-------------|-------------|-------------|
| Number                | 3665        | 10581       | 10265       | 7331        | 5378        |
| Rate<br>(Strokes/min) | 76          | 176         | 171         | 122         | 90          |

**Table 2**

Minimum values of TBs and Polarization Corrected Temperature (PCTs) for the GMI overpass of Naples hailstorm at 08:47 UTC on 5 September 2015. The corresponding instantaneous field of view (IFOV) size is also indicated.

| GMI<br>channels | min TB<br>value (K) | IFOV<br>(km <sup>2</sup> ) |
|-----------------|---------------------|----------------------------|
| 18.7 GHz V      | 158                 | 11x18                      |
| 23.8 GHz        | 138                 | 9.2x15                     |
| 36.5 GHz PCT    | 100                 | 8.6x14                     |
| 89.0 GHz PCT    | 68                  | 4.4x7.2                    |
| 166 GHz H       | 86                  | 4.4x7.2                    |
| 166 GHz V       | 87                  | 4.4x7.2                    |
| 183.31±3 GHz    | 94                  | 4.4x7.2                    |
| 183.31±7 GHz    | 92                  | 4.4x7.2                    |

**Table 3**

Minimum values of TBs for the MHS overpasses of Naples hailstorm at 08:34 UTC and 09:28 UTC on 5 September 2015. The corresponding IFOV size is also indicated.

| Satellite | Min<br>89<br>GHz | Min<br>157<br>GHz | Min<br>183±1<br>GHz | Min<br>183±3<br>GHz | Min<br>183±7<br>GHz | IFOV<br>(km <sup>2</sup> ) |
|-----------|------------------|-------------------|---------------------|---------------------|---------------------|----------------------------|
| MetOp-A   | 121 K            | 111 K             | 146 K               | 123 K               | 118 K               | 34.4x21.4                  |
| MetOp-B   | 151 K            | 129 K             | 156 K               | 137 K               | 134 K               | 28.9x19.7                  |



**Table 4**

Analysis of PFs found in 26 months of global observations (03/2014-04/2016, <http://atmos.tamucc.edu/trmm/data/gpm>) based on minimum TB and PCT values. Second column shows the ranking of Naples hailstorm (for each TB or PCT) with respect to over 15 millions (15,274,291) global PFs. Third to sixth column show the geographical distribution (in terms of number and %) of the PFs with TB and PCT minimum values equal to or lower than those found for the Naples hailstorm.

| GMI TB or PCT | Ranking | TRMM<br>Area (no<br>CONUS) | Mediterranean<br>Area | CONUS       | Other<br>regions |
|---------------|---------|----------------------------|-----------------------|-------------|------------------|
| 19 GHz V-Pol  | 1       | -                          | 1 (100%)              | -           | -                |
| 23 GHz        | 2       | -                          | 1 (50%)               | 1 (50%)     | -                |
| 37 GHz PCT    | 4       | -                          | 1 (25%)               | 2 (50%)     | 1 (25%)          |
| 89 GHz PCT    | 98      | 80 (81.63%)                | 3 (3.06%)             | 12 (12.24%) | 3 (3.06%)        |
| 166 GHz V-Pol | 1798    | 1740 (96.77%)              | 6 (0.33%)             | 33 (1.83%)  | 19 (1.06%)       |
| 183±3 GHz     | 1745    | 1704 (97.65%)              | 4 (0.23%)             | 23 (1.32%)  | 14 (0.80%)       |
| 183±7 GHz     | 2219    | 2161 (97.39%)              | 6 (0.27%)             | 32 (1.44%)  | 20 (0.90%)       |

## Figure Caption List

**Fig. 1.** Hailstone bombing observed by a boat 2 km off the coast, north of Procida Island (40.78°N, 14.02°E) around 09:00 UTC (left panel). Baseball-size hailstones (right panel). Photographs extracted from the videos available at

[http://www.youreporter.it/video\\_Eccezionale\\_tempesta\\_di\\_grandine\\_nel\\_golfo\\_di\\_Napoli](http://www.youreporter.it/video_Eccezionale_tempesta_di_grandine_nel_golfo_di_Napoli) (courtesy of Rosario Chiocca) and at <https://www.youtube.com/watch?v=yarARzbkjl4>.

**Fig. 2.** Sequence of eight MSG snapshots depicting different storm evolution phases at, from left to right, 06:12 UTC, 06:32 UTC, 07:12 UTC, 07:52 UTC, 08:37 UTC, 08:47 UTC, 09:32 UTC, 10:27 UTC. Red circles indicate early development of the cell. A time-line at the bottom of the eight panels indicates key features in the storm development and observations available throughout the storm evolution.

**Fig. 3.** Cloud features in the early stages: a) Time series of Updraft Top Temperature (UTT); b) temporal rate of change of UTT; c) cloud top divergence (CTD); d) stroke rate density, calculated as the number of strokes recorded in a 5 min interval per unit area.

**Fig. 4.** Map of LINET strokes registered between 06:12 UTC and 11:00 UTC over the area swept by the hailstorm (latitude: 40.5°N÷41.5°N; longitude: 12.5°E÷15.5°E) on 5 September 2015, with colours from red to blue representing the strokes registered within each hour. The black crosses represent strokes registered at the same time outside the area of interest.

**Fig. 5.** Temporal evolution of LINET strokes between 06:00 UTC and 11:00 UTC. Top panel: Number of each type of strokes registered every minute over the area swept by the hailstorm. Middle panel: fraction per minute of each type of strokes. Bottom panel: rate density and mean height per minute of IC+ strokes only.

**Fig. 6.** Sequence of reflectivity factor maps collected by the Monte il Monte radar from 08:30 UTC to 10:55 UTC highlighting the evolution of the hailstorm. Measurements are collected at an elevation angle of 1.5°. The black line superimposed over reflectivity factor map at 08:45 UTC corresponds to 209.5° azimuth.

**Fig 7.** Vertical cut at the azimuth angle of 209.5° of reflectivity factor ( $Z_h$ , top), differential reflectivity ( $Z_{dr}$ , middle), and copolar correlation coefficient ( $\rho_{hv}$ , bottom) of the volume scan collected at 08:45 UTC (nominal) by the Monte il Monte radar. A ground profile is also shown.

**Fig. 8.** GMI orbit 8630 on 5 September 2015. Left panel: TB in the 166 GHz H-polarization channel, with the width of Ku and Ka swaths superimposed (green and magenta lines respectively).

Right panel: same as in left panel, with a zoom over the area of interest. The direction of three cross-sections of the storm, which will be analyzed in this study, are also shown in this panel as solid and dashed black lines for cross-section “A” (Ku ray 21 – Ka ray 9) and “B” (Ku ray 15 – Ka ray 3), and dashed magenta line for cross section “C” (Ku/Ka scan 4941).

**Fig. 9.** TBs from GMI overpass at 08:47 UTC on 5 September 2015. From left to right, first row 18.7 GHz V, 36.5 GHz V/H, second row 89.0 GHz V/H, 166 GHz V, third row 166 GHz H,  $183.31 \pm 3$  GHz,  $183.31 \pm 7$  GHz.

**Fig. 10.** TB difference between vertical and horizontal polarization channels (V–H) at 89 GHz (left panel) and 166 GHz (right panel) from GMI overpass at 08:47 UTC on 5 September 2015. Contour lines of TB in the vertical polarization are also drawn for 89 GHz V-Pol and 166 GHz V-Pol. Dashed lines for 166 GHz V-Pol correspond to 125 K, 175 K and 225 K, while the inner dashed line for 89 GHz V-Pol corresponds to 75 K.

**Fig. 11.** TBs from MHS overpasses at 08:34 UTC (MetOp-A, first row) and 09:28 UTC (MetOp-B, second row) on 5 September 2015. From left to right, 89 GHz, 157 GHz V/H, 190 GHz.

**Fig. 12.** DPR along-track sections: section A (left column) and section B (right column) of measured reflectivity ( $Z_m$ ) at Ku (first row) and Ka (matched scan, MS) (second row). GMI TBs for 4 window channels (V-Pol) and 183.31 GHz channels, corrected for parallax effects, are superimposed. On top of each panel the DPR scan number along the cross-section is indicated. See Fig. 8 as reference for the position of section A and B.

**Fig. 13.** DPR across-track section C of Ku measured reflectivity ( $Z_m$ ). GMI TBs 4 window channels (V-Pol) and 183.31 GHz channels, corrected for parallax effects, are superimposed. On top the DPR Ku-band ray number along the cross-section is indicated. See Fig. 8 as reference for the position of section C.

**Fig. 14.** Map of LINET strokes (IC and CG) during a 4 min time interval around 08:47 UTC superimposed over GMI TB at 19 GHz V-Pol (top panel), over DPR Ku-band median  $Z_m$  (bottom left panel) and over GR reflectivity at 2.5° elevation at nominal 08:45 UTC (bottom right panel). The DPR-Ku ray 21 (cross-section A) and scan 4941 (cross-section C) are shown in pink.

**Fig. 15.** DPR and GR cross-section A (left panels) and C (right panels) with LINET strokes (IC+ and IC-) registered in 4 min around 08:47 UTC within a circular area of 2.5 km radius around each radar pixel. Top panels: Ku measured reflectivity  $Z_m$  (dBZ). Middle panels: GR C-band reflectivity  $Z_h$  (dBZ) Bottom Panels: GR measured C-band differential reflectivity  $Z_{dr}$  (dB).



**Figure 1:** Hailstone bombing observed by a boat 2 km off the coast, north of Procida Island ( $40.78^{\circ}\text{N}$ ,  $14.02^{\circ}\text{E}$ ) around 09:00 UTC (left panel). Baseball-size hailstones (right panel). Photographs extracted from the videos available at [http://www.youreporter.it/video\\_Eccezionale\\_tempesta\\_di\\_grandine\\_nel\\_golfo\\_di\\_Napoli](http://www.youreporter.it/video_Eccezionale_tempesta_di_grandine_nel_golfo_di_Napoli) (courtesy of Rosario Chiocca) and at <https://www.youtube.com/watch?v=yarARzbkjl4>.

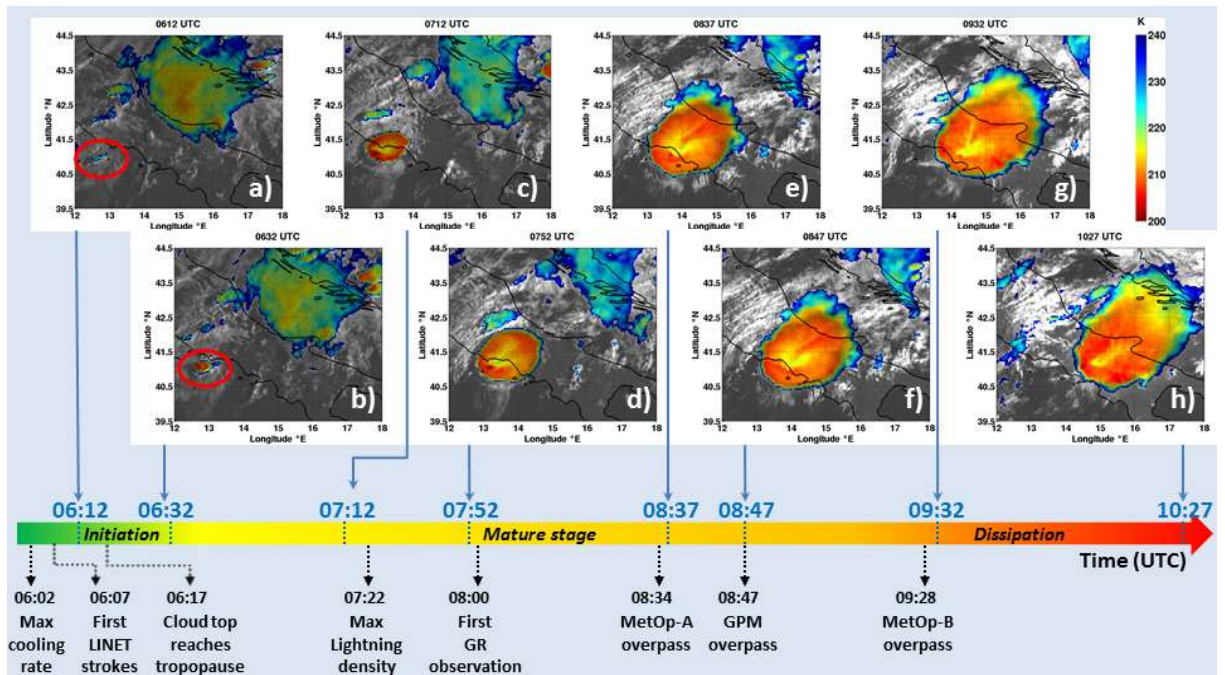


**Figure 2:** Sequence of eight MSG snapshots depicting different storm evolution phases at, from left to right, 06:12 UTC, 06:32 UTC, 07:12 UTC, 07:52 UTC, 08:37 UTC, 08:47 UTC, 09:32 UTC, 10:27 UTC. Red circles indicate early development of the cell. A time-line at the bottom of the eight panels indicates key features in the storm development and observations available throughout the storm evolution.

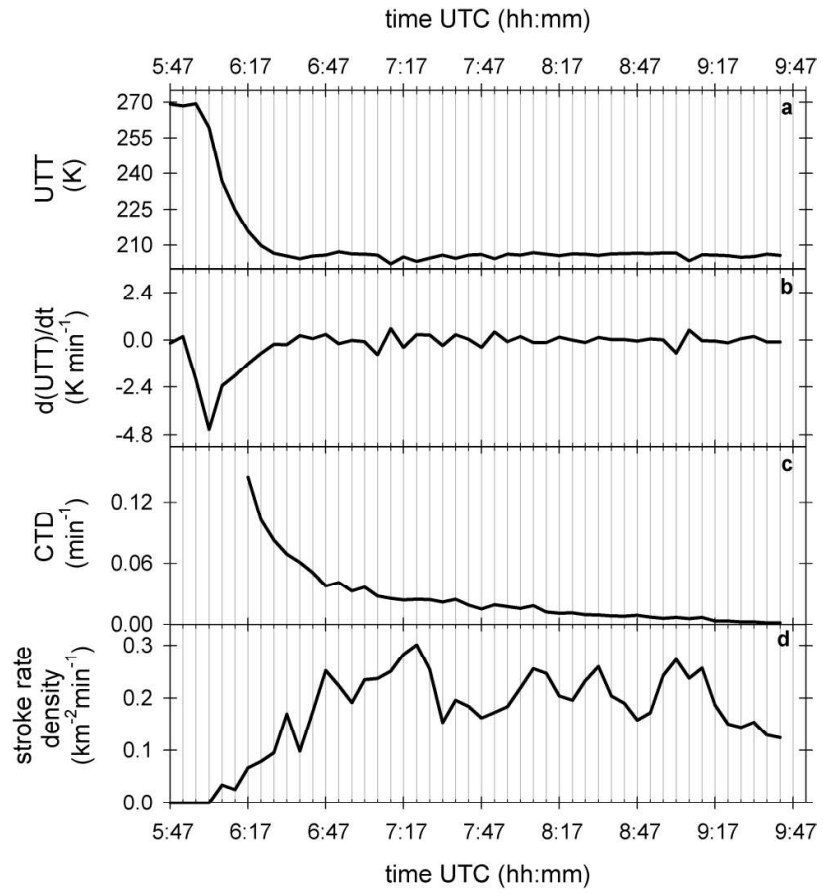


**Figure 3:** Cloud features in the early stages: a) Time series of Updraft Top Temperature (UTT); b) temporal rate of change of UTT; c) cloud top divergence (CTD); d) stroke rate density, calculated as the number of strokes recorded in a 5 min interval per unit area.

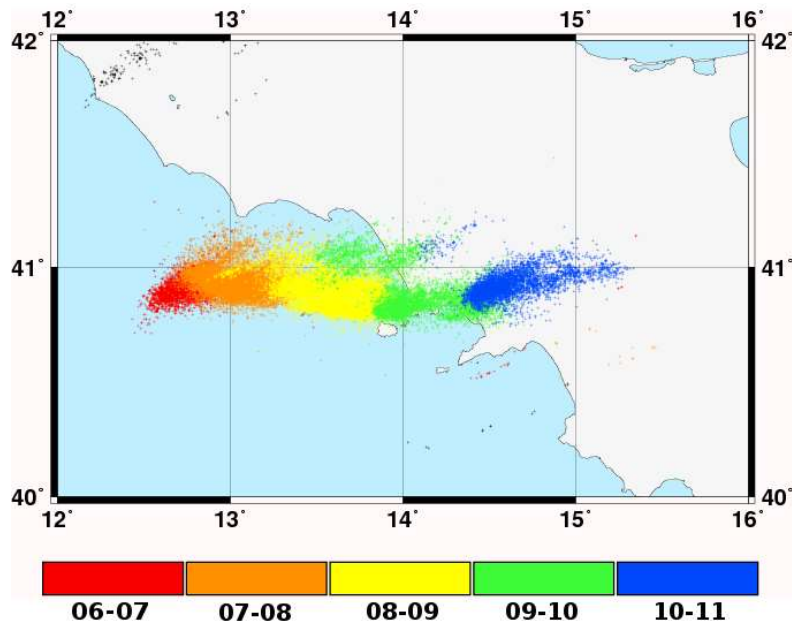


**Figure 4:** Map of LINET strokes registered between 06:12 UTC and 11:00 UTC over the area swept by the hailstorm (latitude: 40.5°N÷41.5°N; longitude: 12.5°E÷15.5°E) on 5 September 2015, with colours from red to blue representing the strokes registered within each hour. The black crosses represent strokes registered at the same time outside the area of interest.



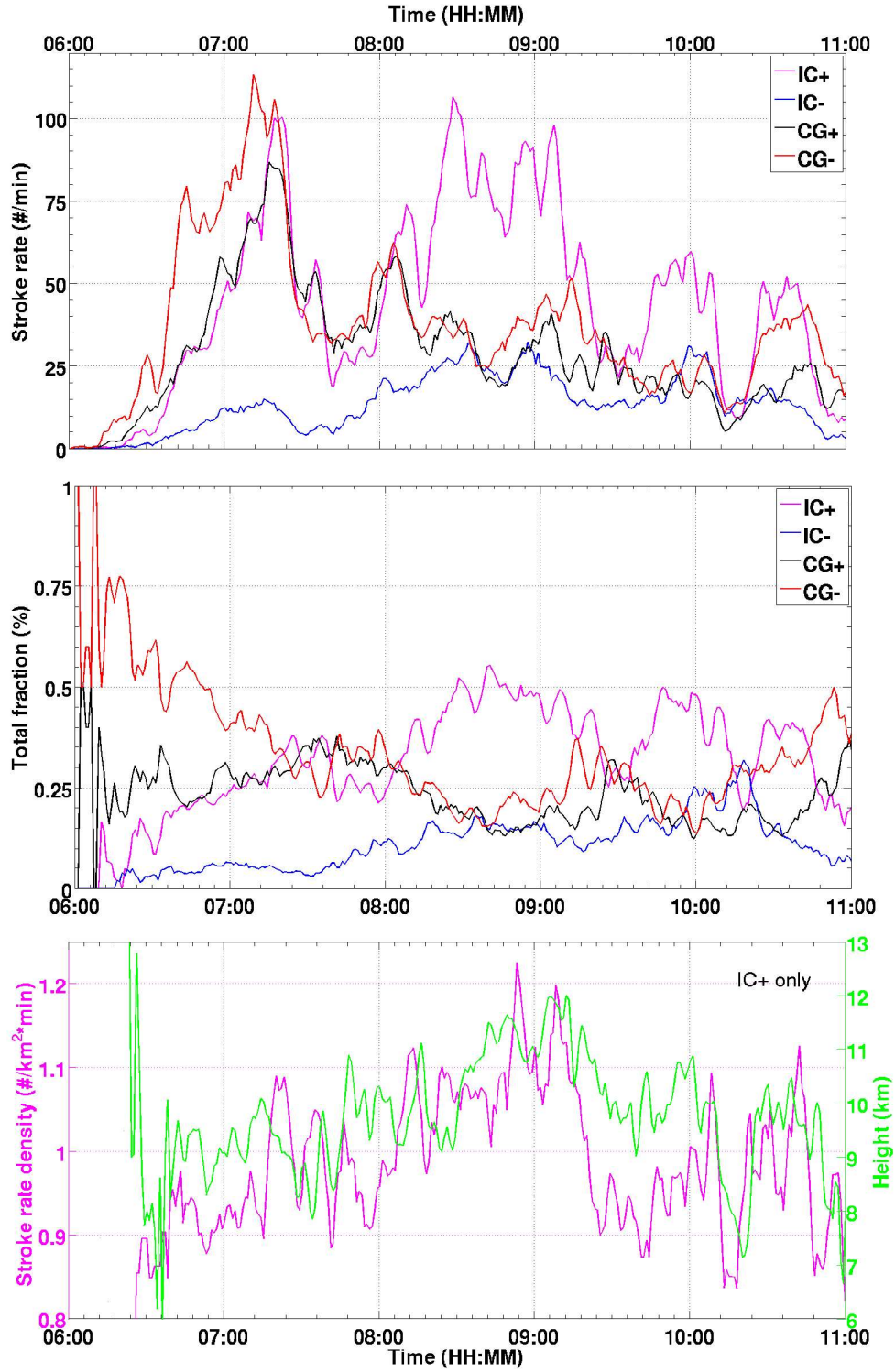


**Figure 5:** Temporal evolution of LINET strokes between 06:00 UTC and 11:00 UTC. Top panel: Number of each type of strokes registered every minute over the area swept by the hailstorm. Middle panel: fraction per minute of each type of strokes. Bottom panel: rate density and mean height per minute of IC+ strokes only.



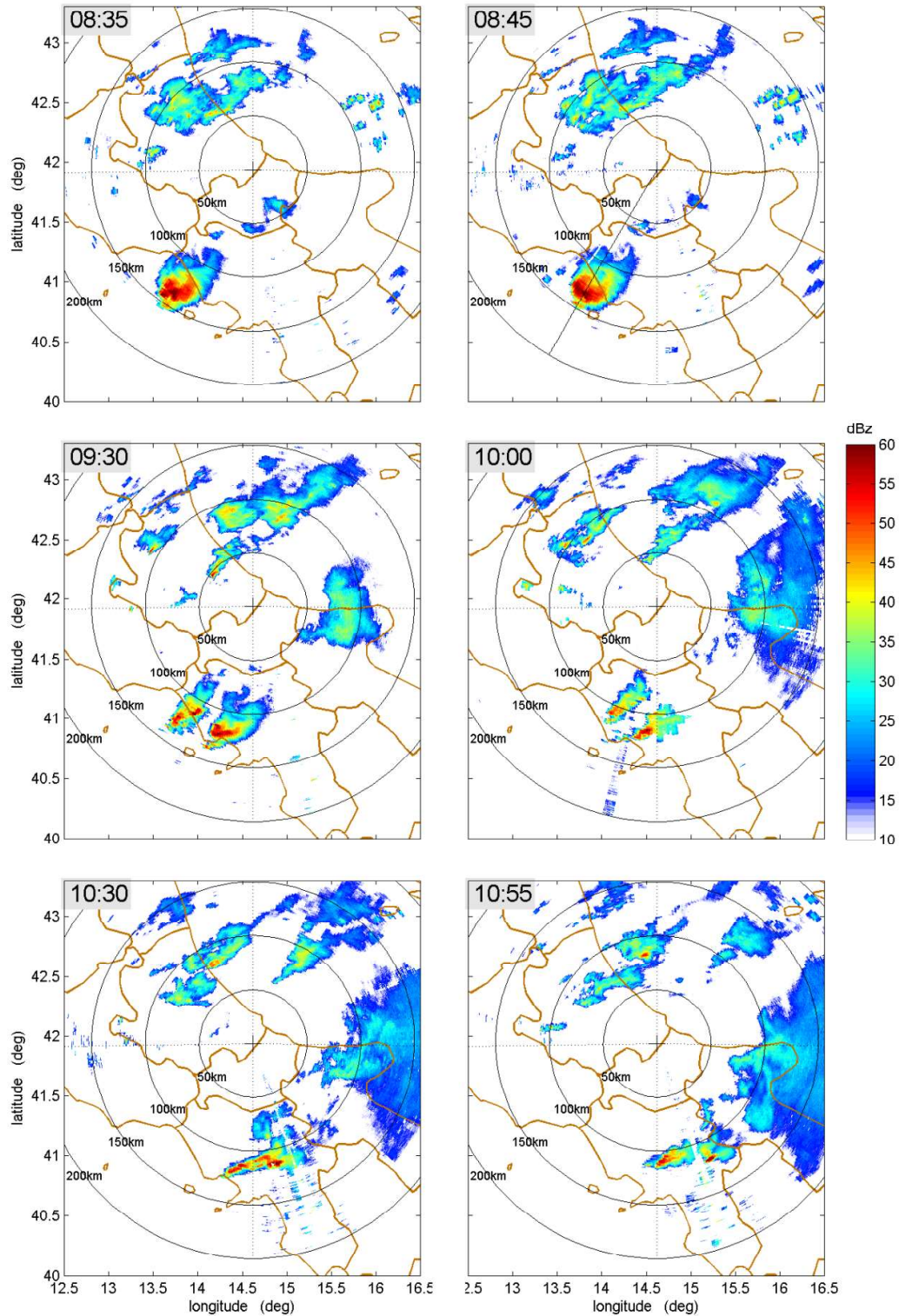


**Figure 6:** Sequence of reflectivity factor maps collected by the Monte il Monte radar from 08:30 UTC to 10:55 UTC highlighting the evolution of the hailstorm. Measurements are collected at an elevation angle of  $1.5^\circ$ . The black line superimposed over reflectivity factor map at 08:45 UTC corresponds to  $209.5^\circ$  azimuth.

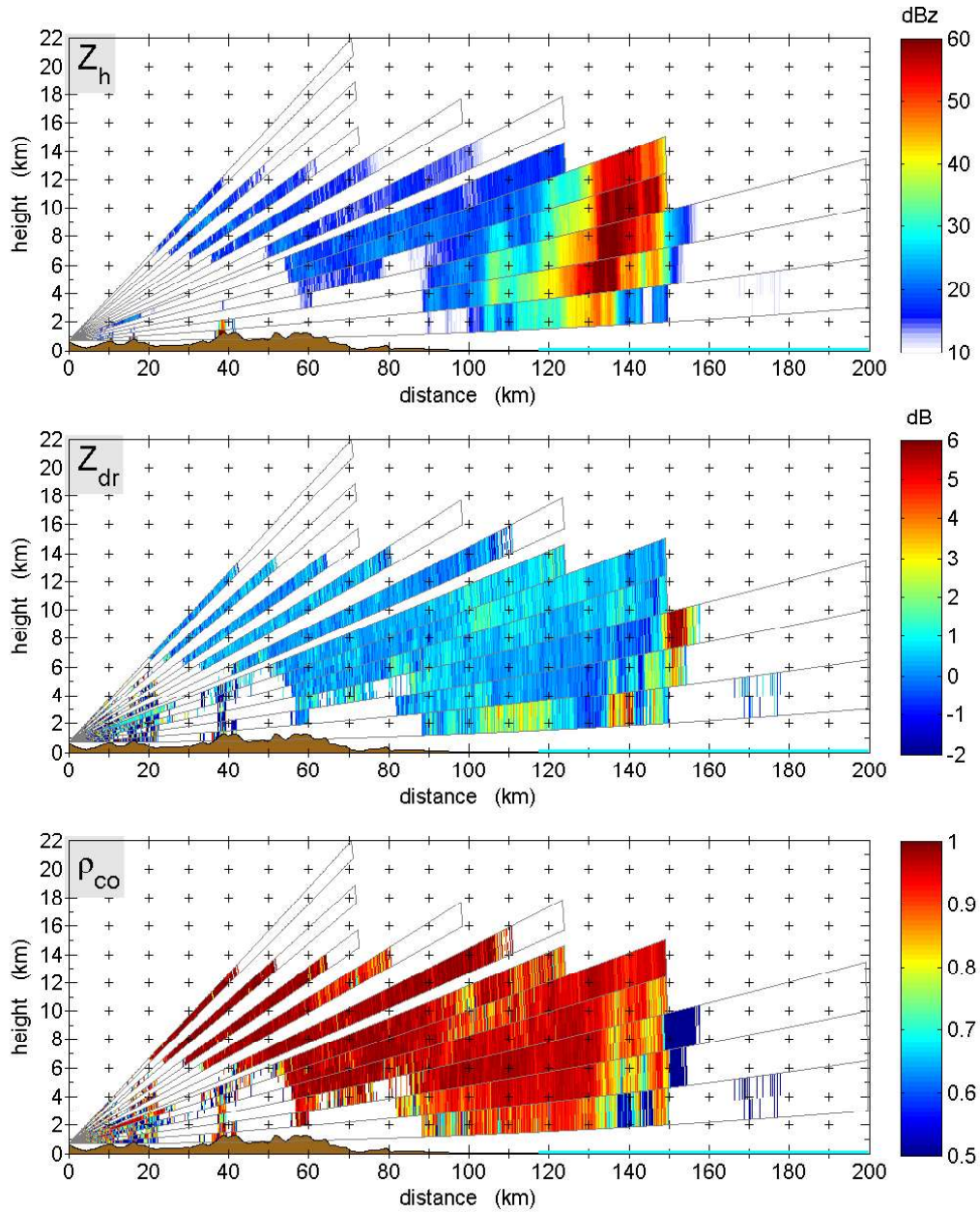


**Figure 7:** Vertical cut at the azimuth angle of 209.5° of reflectivity factor ( $Z_h$ , top), differential reflectivity ( $Z_h$ , middle), and copolar correlation coefficient ( $\rho_{hv}$ , bottom) of the volume scan collected at 08:45 UTC (nominal) by the Monte il Monte radar. A ground profile is also shown.

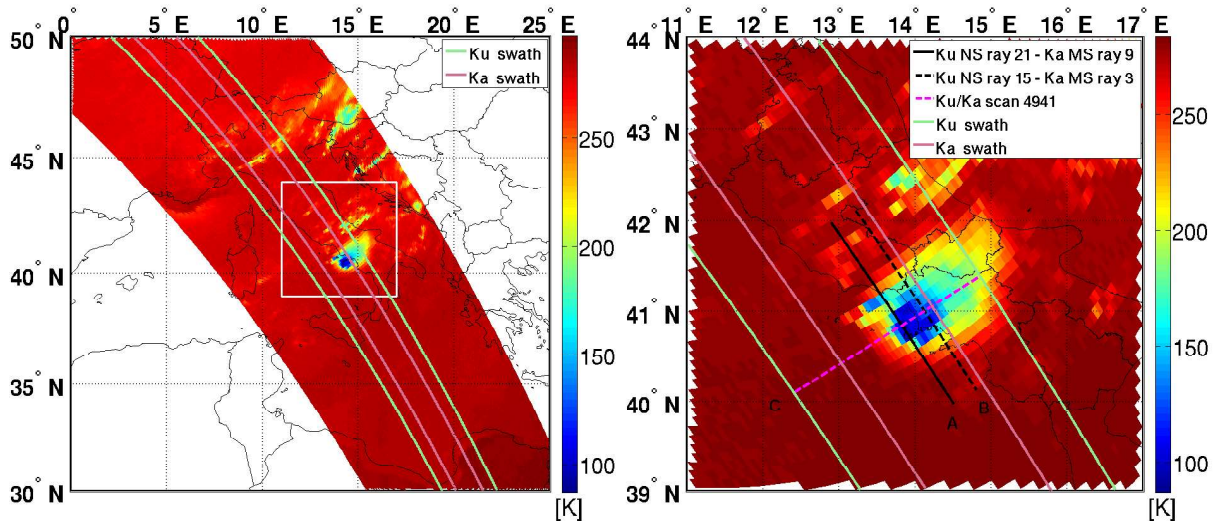


**Figure 8:** GMI orbit 8630 on 5 September 2015. Left panel: TB in the 166 GHz H-polarization channel, with the width of Ku and Ka swaths superimposed (green and magenta lines respectively). Right panel: same as in left panel, with a zoom over the area of interest. The direction of three cross-sections of the storm, which will be analyzed in this study, are also shown in this panel as solid and dashed black lines for cross-section “A” (Ku ray 21 – Ka ray 9) and “B” (Ku ray 15 – Ka ray 3), and dashed magenta line for cross section “C” (Ku/Ka scan 4941).



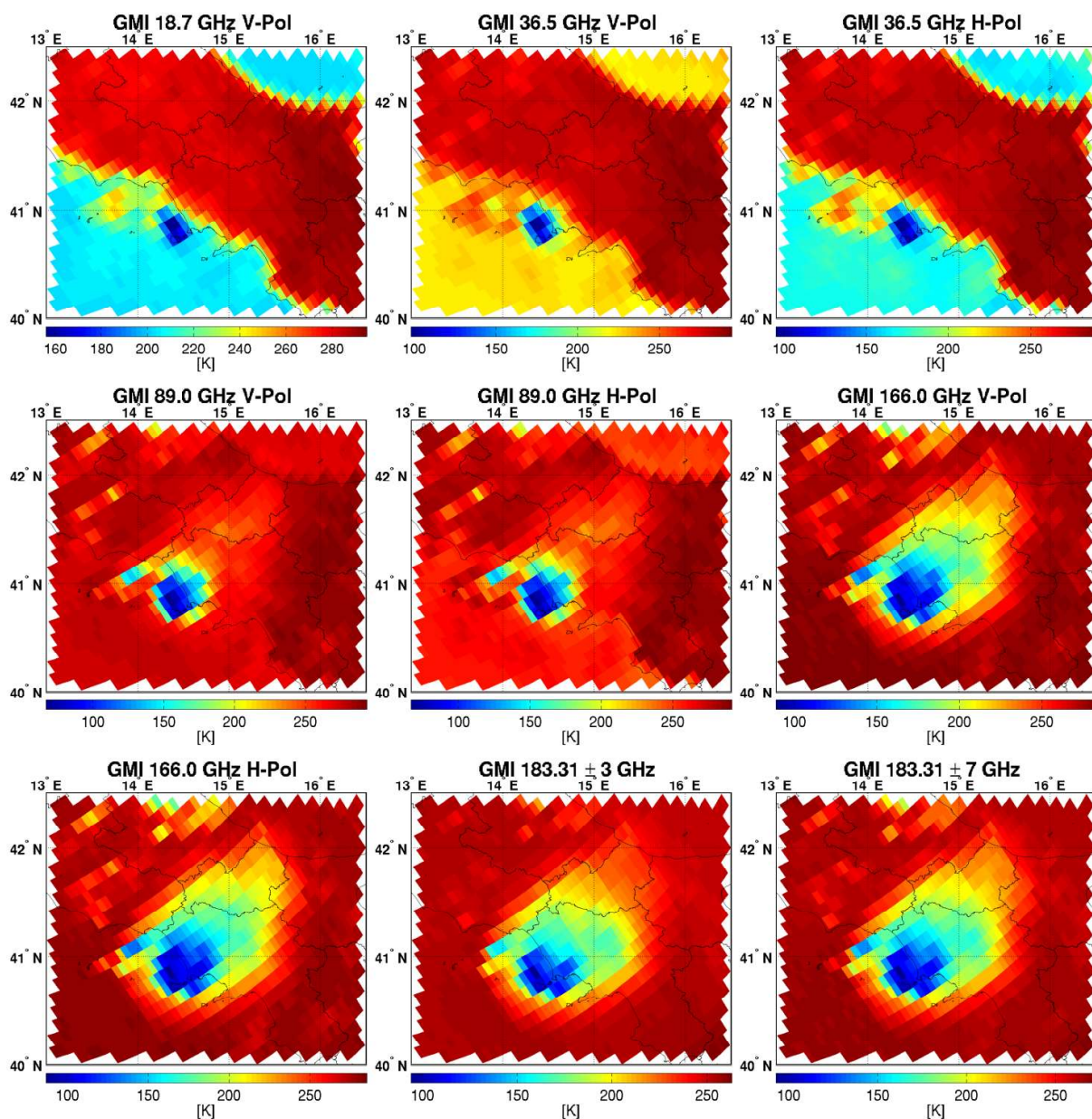


**Figure 9:** TBs from GMI overpass at 08:47 UTC on 5 September 2015. From left to right, first row 18.7 GHz V, 36.5 GHz V/H, second row 89.0 GHz V/H, 166 GHz V, third row 166 GHz H,  $183.31 \pm 3$  GHz,  $183.31 \pm 7$  GHz.

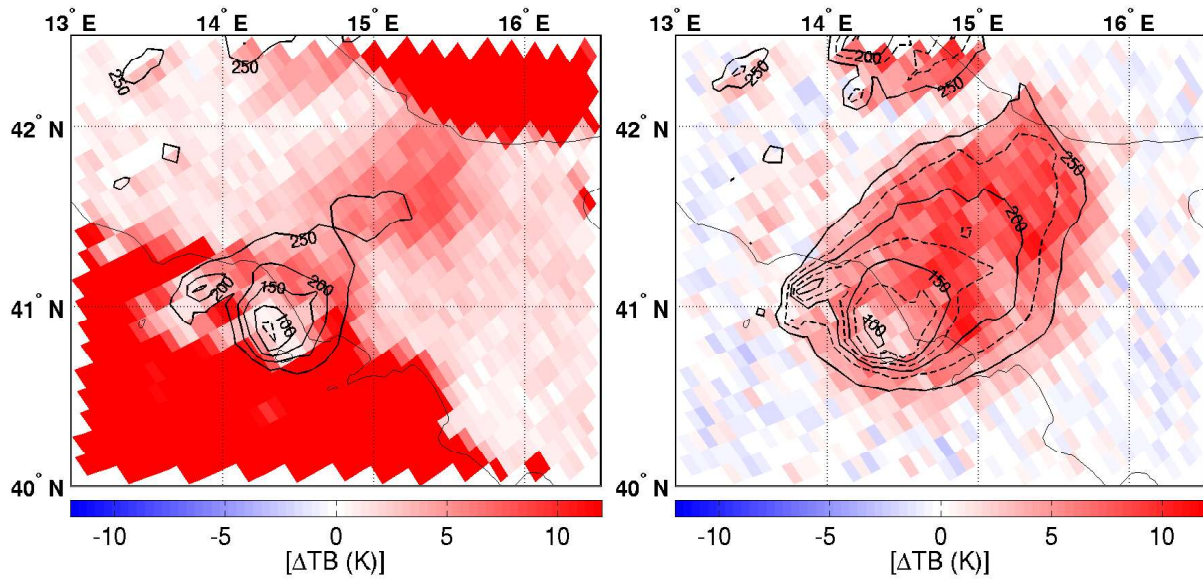


**Figure 10:** TB difference between vertical and horizontal polarization channels (V–H) at 89 GHz (left panel) and 166 GHz (right panel) from GMI overpass at 08:47 UTC on 5 September 2015. Contour lines of TB in the vertical polarization are also drawn for 89 GHz V-Pol and 166 GHz V-Pol. Dashed lines for 166 GHz V-Pol correspond to 125 K, 175 K and 225 K, while the inner dashed line for 89 GHz V-Pol corresponds to 75 K.

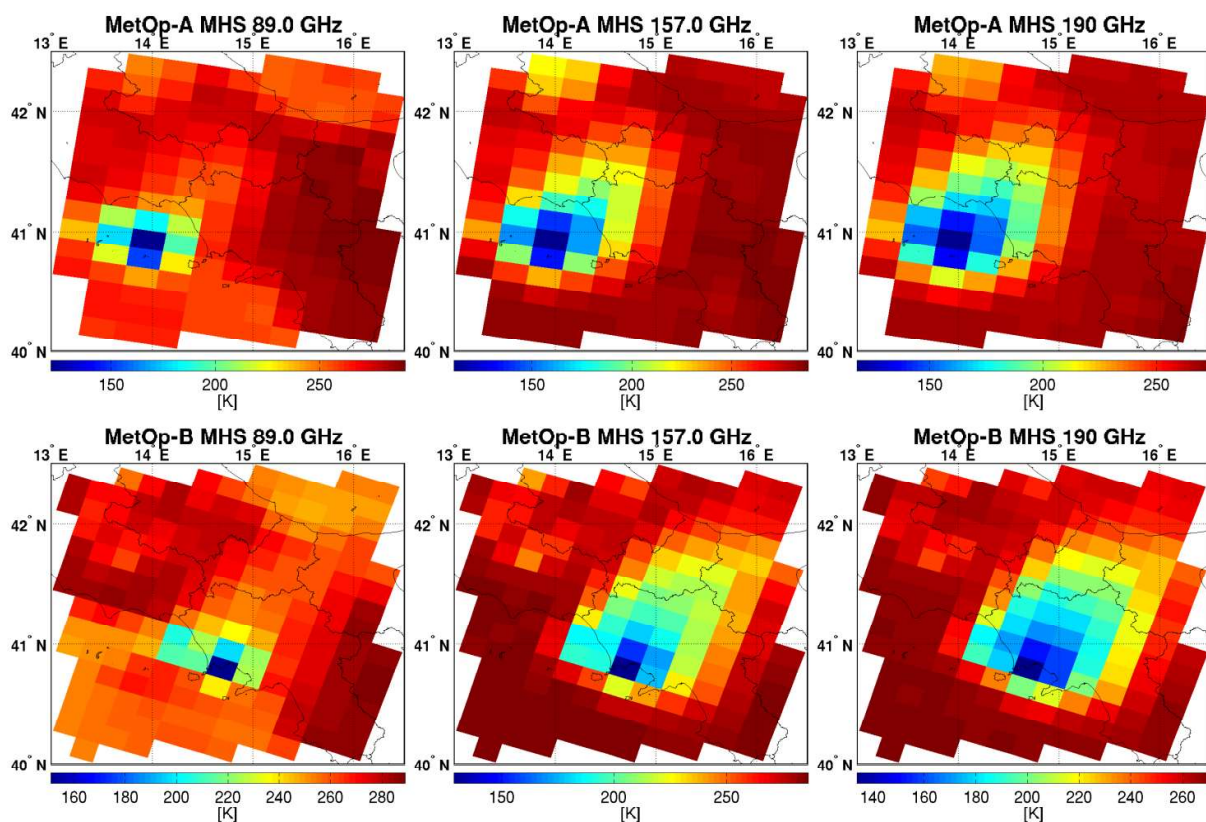


**Figure 11:** TBs from MHS overpasses at 08:34 UTC (MetOp-A, first row) and 09:28 UTC (MetOp-B, second row) on 5 September 2015. From left to right, 89 GHz, 157 GHz V/H, 190 GHz.



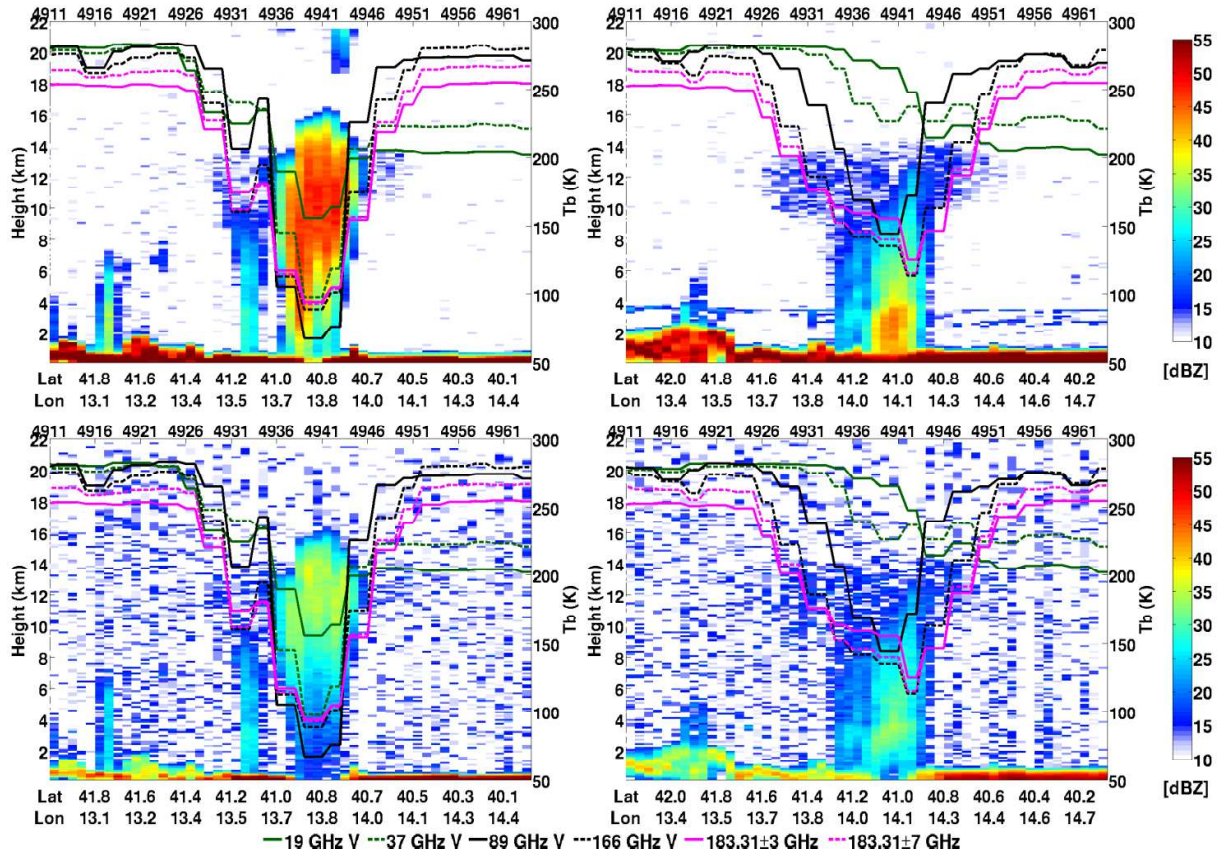


**Figure 12:** DPR along-track sections: section A (left column) and section B (right column) of measured reflectivity ( $Z_m$ ) at Ku (first row) and Ka (matched scan, MS) (second row). GMI TBs for 4 window channels (V-Pol) and 183.31 GHz channels, corrected for parallax effects, are superimposed. On top of each panel the DPR scan number along the cross-section is indicated. See Fig. 8 as reference for the position of section A and B.

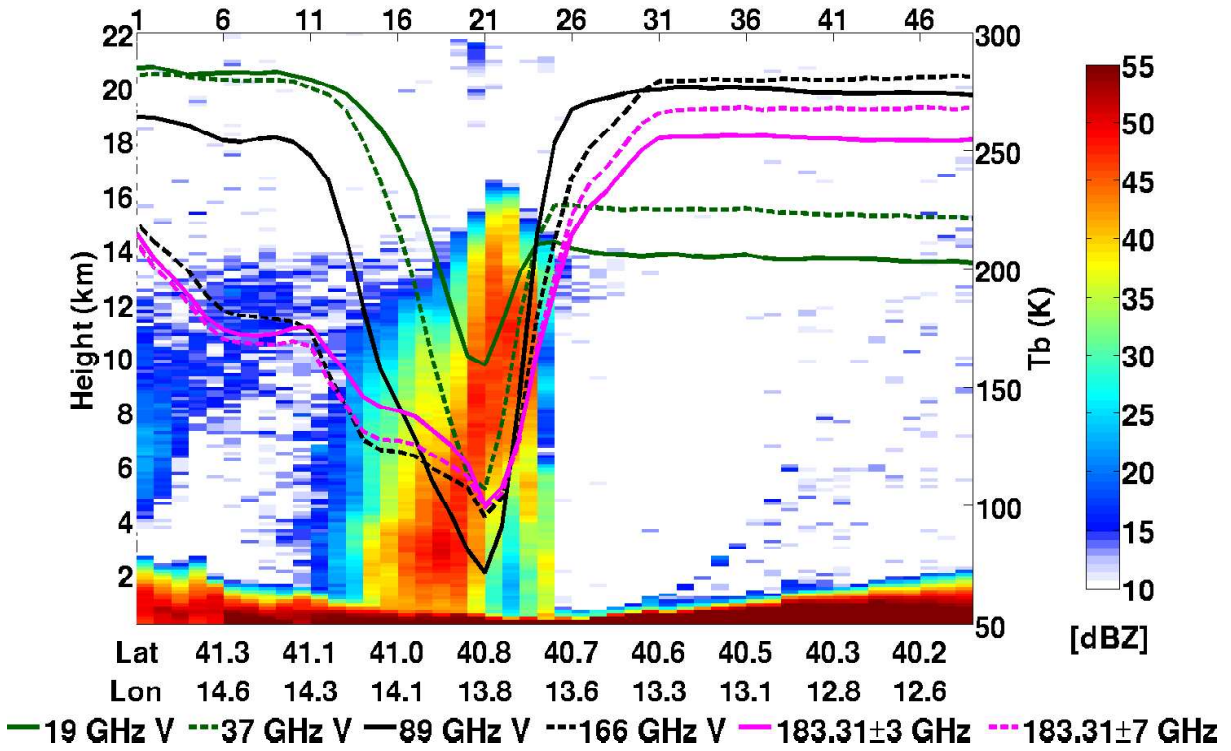


**Figure 13:** DPR across-track section C of Ku measured reflectivity ( $Z_m$ ). GMI TBs 4 window channels (V-Pol) and 183.31 GHz channels, corrected for parallax effects, are superimposed. On top the DPR Ku-band ray number along the cross-section is indicated. See Fig. 8 as reference for the position of section C.

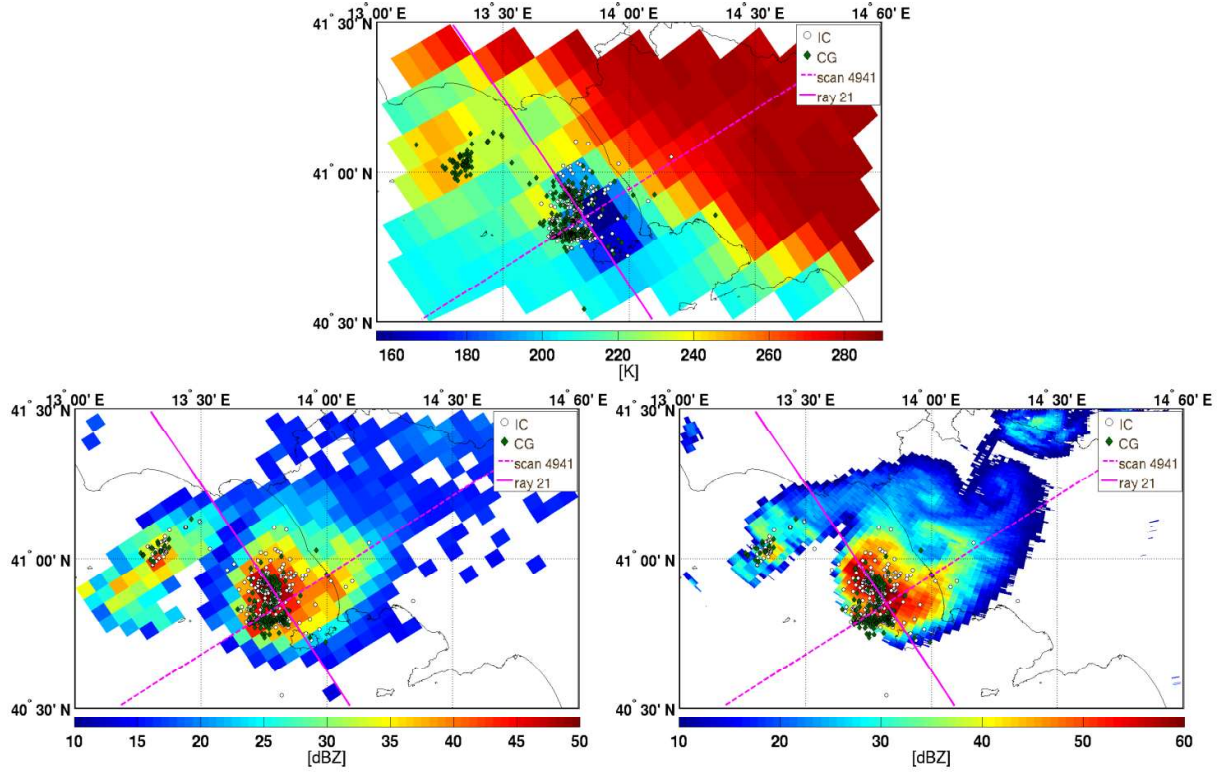


**Figure 14:** Map of LINET strokes (IC and CG) during a 4 min time interval around 08:47 UTC superimposed over GMI TB at 19 GHz V-Pol (top panel), over DPR Ku-band median  $Z_m$  (bottom left panel) and over GR reflectivity at 2.5° elevation at nominal 08:45 UTC (bottom right panel). The DPR-Ku ray 21 (cross-section A) and scan 4941 (cross-section C) are shown in pink.

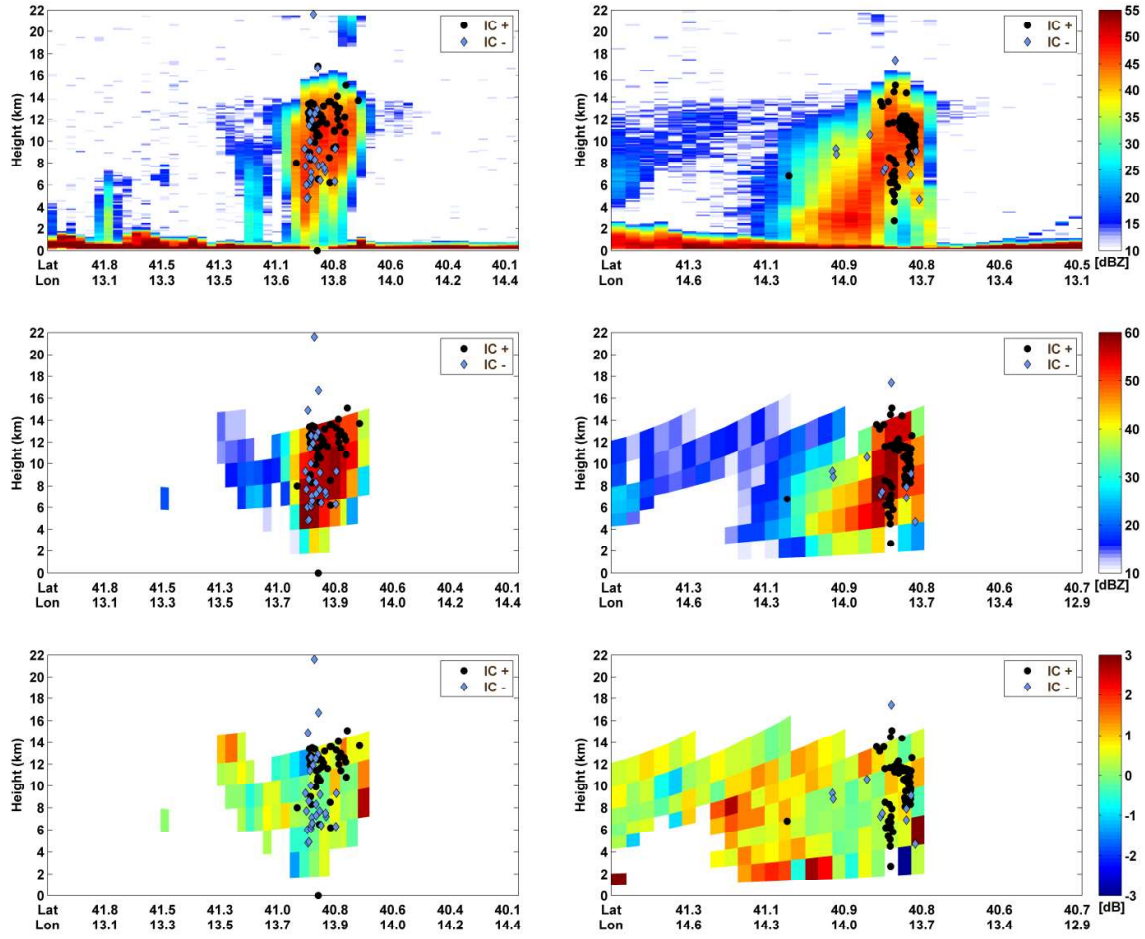


**Figure 15:** DPR and GR cross-section A (left panels) and C (right panels) with LINET strokes (IC+ and IC-) registered in 4 min around 08:47 UTC within a circular area of 2.5 km radius around each radar pixel. Top panels: Ku measured reflectivity  $Z_m$  (dBZ). Middle panels: GR C-band reflectivity  $Z_h$  (dBZ) Bottom Panels: GR measured C-band differential reflectivity  $Z_{dr}$  (dB).